

The galaxy counterpart of the high-metallicity and 16 kpc impact parameter DLA towards Q 0918+1636 - a challenge to galaxy formation models?

J. Sommer-Larsen^{1,2,3*} & J. P. U. Fynbo¹

¹Dark Cosmology Centre, Niels Bohr Institute, Copenhagen University, Juliane Maries Vej 30, 2100 Copenhagen O, Denmark

²Excellence Cluster Universe, Technische Universität München, Boltzmannstrasse 2, 85748 Garching, Germany

³Marie Kruses Skole, Stavsholtvej 29-31, DK-3520 Farum, Denmark

31 July 2018

ABSTRACT

The quasar Q0918+1636 ($z=3.07$) has an intervening high-metallicity Damped Lyman- α Absorber (DLA) along the line of sight, at a redshift of $z=2.58$. The DLA is located at a large impact parameter of 16.2 kpc, and despite this large impact parameter it has a very high metallicity (consistent with solar). In this paper it is investigated whether a novel type of galaxy formation models, based on hydrodynamical/gravitational TreeSPH simulations invoking a new SNII feedback prescription, the Haardt & Madau (2012) ultra-violet background radiation (UVB) field and explicit treatment of UVB self-shielding effects, can reproduce the observed characteristics of the DLA. Effects of UV radiation from young stellar populations in the galaxy, in particular in the photon energy range 10.36-13.61 eV (relating to Sulfur II abundance), are also considered in the analysis. It is found that a) for $L \sim L_*$ galaxies (at $z=2.58$), about 10% of the sight-lines through the galaxies at impact parameter $b=16.2$ kpc will display a Sulfur II column density of $N(\text{SII}) \geq 10^{15.82} \text{ cm}^{-2}$ (the observed value for the DLA), and b) considering only cases where a near-solar metallicity will be detected at 16.2 kpc impact parameter, the (Bayesian) probability distribution of galaxy star formation rate (SFR) peaks near the value observed for the DLA galaxy counterpart of $27_{-9}^{+20} M_{\odot}/\text{yr}$. It is argued, that the bulk of the α -elements, like Sulfur, traced by the high metal column density, $b=16.2$ kpc absorption lines, have been produced by evolving stars in the inner galaxy, and subsequently transported outward by galactic winds.

Key words: galaxies: formation – galaxies: high-redshift – galaxies: ISM – quasars: absorption lines – cosmology: observations – cosmology: theory

1 INTRODUCTION

Using optical and near-infrared imaging and spectroscopy, galaxies at redshifts $z \gtrsim 1$ can be detected in two main ways: a) in absorption against the light of background QSOs, e.g., Weymann et al. (1981); Wolfe et al. (2005) and b) in emission, e.g., Giavalisco (2002); Shapley (2011). However, combining the information from absorption and emission lines is still a poorly developed field. Although more than 10 000 of the so-called Damped Lyman- α Absorbers (DLAs) have been found so far (Prochaska & Stephane 2004; Prochaska & Wolfe 2009; Noterdaeme et al. 2012b), and despite some progress (e.g., Møller et al. 2002) in finding their galaxy counterparts, we still have less than a dozen examples of such absorption selected galaxies (Krogager et al. 2012, see also Rauch et al. 2008, Rauch & Haehnelt 2011 and Schulze et al. 2012).

In this paper, the main focus will be on the interesting case of

a DLA at $z = 2.583$, with a potential galaxy counterpart located such, that the QSO line-of-sight (los) relative to the galaxy corresponds to a very large impact parameter of 16.2 kpc. At the same time, the gas abundance of non-refractory elements, such as Zinc and, to some extent, also Sulfur is close to solar, see Fynbo et al. (2011) for details. Further investigations of the $z = 2.583$ DLA galaxy were carried out by Fynbo et al. (2013). They performed deep multi-band imaging of the galaxy using HST, NOT/Alfosc and NOT/NotCam. From SED fitting they derived a star-formation rate (SFR) of $27_{-9}^{+20} M_{\odot} \text{ yr}^{-1}$ assuming a Chabrier (2003) initial mass function (IMF). To search for emission lines from the DLA galaxy, VLT/X-Shooter spectroscopy was also performed. A range of emission lines were clearly detected, with the [OIII] $\lambda 5007$ emission line having the highest S/N ratio. This line is just $36 \pm 20 \text{ km s}^{-1}$ blue-shifted compared to the center of the low-ionization DLA absorption lines, very strongly suggesting a physical connection between the DLA absorption region and the (potential) DLA galaxy.

* E-mail: jslarsen@astro.ku.dk

Other emission lines detected (albeit at somewhat lower S/N) include the H α , H β , [OIII] λ 4960, and [OII] λ 3727 lines.

From a theoretical point of view, it is of great interest to test whether state-of-the-art galaxy formation models can reproduce, even as an extreme case, single- or multi-component galaxies displaying such a large metal abundance at 16.2 kpc galactocentric distance. And, if so, it is of interest to calculate the probability distribution of (semi-)observable quantities, such as absolute visual magnitude, M_V , or star-formation rate, SFR, to check whether the properties observationally inferred for the $z = 2.583$ DLA galaxy are in fact “likely”.

To address these questions, a large number of new galaxy formation simulations have been performed, using a hydrodynamical/gravitational galaxy formation code with a novel implementation of state-of-the-art feedback models. In addition, a previously performed cosmological simulation has been re-analyzed, to further address the above issues. The results obtained have been combined with published $z \sim 2.25-3$ luminosity functions to calculate DLA galaxy probability distributions.

In this paper, details of the simulations and the results obtained are presented. The paper is organized as follows: The code and the simulations are described in section 2, and the results obtained are presented in section 3 and discussed in section 4. In section 5 it is analyzed how the high metallicity gas in outer galaxy was enriched, and, finally, section 6 constitutes the conclusion.

In the appendix, observational models of $z=2.58$ luminosity functions, as well as procedures of extinction correction are described.

2 THE HYDRODYNAMICAL/GRAVITATIONAL CODE AND THE SIMULATIONS

The code used for the simulations is a significantly improved version of the TreeSPH code we have used previously for galaxy formation simulations (Sommer-Larsen, Götz & Portinari 2003): Full details will be given in a forthcoming paper; here we just summarize the main improvements (1) In lower resolution regions (which will always be present in cosmological CDM simulations) an improvement in the numerical accuracy of the integration of the basic equations is obtained by solving the entropy equation rather than the thermal energy equation — we have adopted the “conservative” entropy equation solving scheme suggested by Springel & Hernquist (2002). (2) High-density gas is, subject to a number of conditions, turned into stars in a probabilistic way, and in a star-formation event, an SPH particle is converted fully into a star particle. The star-formation threshold density is set to $n_H = 1 \text{ cm}^{-3}$, and the star-formation efficiency is set to 0.1. In conjunction with the new stellar feedback prescription, detailed in subsections 2.3-2.4, this star-formation prescription reproduces the observed Kennicutt-Schmidt law (Kennicutt 1998) quite well — full detail will be given in a forthcoming paper. (3) Non-instantaneous recycling of gas and heavy elements is described through probabilistic “decay” of star particles back to SPH particles as discussed by Lia, Portinari & Carraro (2002a). In a decay event a star particle is converted fully into an SPH particle. (4) Non-instantaneous chemical evolution tracing 10 elements (H, He, C, N, O, Mg, Si, S, Ca and Fe) has been incorporated in the code following Lia et al. (2002a,b); the algorithm includes supernovae of type II and type Ia, and mass loss from stars of all masses. Metal diffusion in Lia et al. was included with a diffusion coefficient κ derived from models of the expansion of individual supernova remnants. A much more

important effect in the present simulations, however, is the redistribution of metals (and gas) by means of star-burst driven “galactic super-winds” (see point 6). This is handled self-consistently by the code, so we set $\kappa=0$ in the present simulations. (5) Atomic radiative cooling depending both on the metal abundance of the gas and on the meta-galactic UV field (UVB), modeled after Haardt & Madau (2012), is invoked. Radiative transfer (RT) of the UVB is invoked in the way proposed by Rahmati et al. (2013). In brief, Rahmati et al. (2013) showed that the effect of shielding of the UVB by neutral gas can be well described as a function of redshift and the local gas density. The effect of UVB shielding on the radiative cooling and heating functions is explicitly incorporated using CLOUDY (Ferland et al. 2013) (6) Stellar feedback is incorporated in a new way relative to, e.g., Sommer-Larsen, Götz & Portinari (2003) and Sommer-Larsen, Romeo & Portinari (2005). During the first ~ 3.4 Myr after a stellar population has been born, but before the first core collapse supernovae go off, the massive stars feed radiation energy back to the surrounding ISM. This affects the star formation rate in the surrounding ISM through photo-heating the cold gas, which in turn leads to a decrease in the star-formation rate (Stinson et al. 2013). After ~ 3.4 Myr, the first SNII start exploding and feeding energy back into the ISM. A classic “sub-grid” super-wind model is used to describe the evolution of the surrounding ISM, receiving large amounts of energy.

Both aspects of the stellar feedback are described in detail in the following.

2.1 Stellar feedback

The “over-cooling catastrophe” initially plagued simulations of disk galaxy formation. Fully cosmological numerical galaxy simulations consistently contained a massive central concentration of stars (Navarro & Benz 1991), and the sizes and angular momenta of the disks were too small (e.g., Sommer-Larsen, Götz & Portinari 2003).

Stellar feedback is the favored way of reducing star formation and launching outflows (Scannapieco et al. 2008; Schaye et al. 2010). Semi-analytic models have found that significant amounts of stellar feedback are required to match the low mass end of the luminosity function (Somerville & Primack 1999; Benson et al. 2003; Bower et al. 2006, 2008, 2012). Dutton & van den Bosch (2009) showed that stellar feedback can remove low angular momentum material.

In hydrodynamical simulations, two methods are commonly used to model stellar feedback. One is kinetic feedback that adds velocity kicks to gas particles to remove them from the inner regions of galaxy disks (Springel & Hernquist 2003; Oppenheimer & Davé 2006; Dalla Vecchia & Schaye 2008). The other is thermal feedback in which stars simply heat gas particles and allow the adiabatic work of the particles to push other gas out of the star forming region (Gerritsen & Icke 1997; Thacker & Couchman 2000; Kawata & Gibson 2003; Sommer-Larsen, Götz & Portinari 2003; Stinson et al. 2006).

Since stars form in dense regions, the cooling times of the surrounding gas are short, and without help, the gas will quickly radiate away all the supernova energy (Katz 1992). In real galaxies, the amount of gas necessary to exert a dynamical influence on the ISM is small. In simulations, for resolution reasons, such small amounts of gas are difficult to model, so a common technique has been to turn off radiative cooling for a limited amount of time (Gerritsen & Icke 1997; Thacker & Couchman 2000; Sommer-Larsen, Götz & Portinari 2003; Brook et al. 2004;

Stinson et. al 2006), but see Hopkins et al. (2014) for an alternative approach.

Sommer-Larsen, Götz & Portinari (2003) turned off radiative cooling for the $N_n=50$ SPH particles nearest to the star particle providing the feedback. This was a choice in line with principles of SPH, since all hydrodynamical quantities are smoothed over this number of SPH particles inside of the SPH smoothing kernel. It is easy to show, that for gas of hydrogen number density n_0 being represented by SPH particles of mass m_{SPH} , the radius of the smoothing kernel is given by

$$r = 336 \left(\frac{m_{\text{SPH}}}{10^5 M_\odot} \right)^{1/3} \left(\frac{N_n}{50} \right)^{1/3} n_0^{-1/3} \text{ pc}, \quad (1)$$

where N_n is the number of SPH particles required to be inside the smoothing kernel. When the most massive stars of a newly born stellar population explode as supernovae type II, the true size of the region affected by the supernova feedback is considerably less than the size given by eq. (1), as will be discussed in detail below. This implies that the effect of the supernova feedback on gas near the stellar population is underestimated, due to the SNII energy being smoothed over the entire smoothing kernel. This turns out to hamper the onset of gas outflows, as discussed by, e.g., Stinson et. al (2006).

Motivated by these considerations, in this paper we introduce an approach based on feeding SNII energy back to a region of a size, which is some fixed fraction of the time-dependent radius of a classic super-wind around a star burst, $R_{\text{SW}}(t)$. This is reasonable, since all core collapse supernovae do not go off at the same time — rather the $100 M_\odot$ stars (assumed to be the most massive stars born in a stellar population) go off after about 3.4 Myr, whereas 9 M_\odot stars (assumed to be the least massive stars that explode as SNII), go off after about 34 Myr (Lia, Portinari & Carraro 2002a). During this 30.6 Myr SNII explosion period, the luminosity of the star burst is approximately constant — see further below.

Moreover, as only part of the gas inside of a blast wave or super-wind will remain hot over a period of about 31 Myr, it makes sense to switch off radiative cooling inside only a fraction of the classic super-wind radius, as will be discussed in the following. Firstly, blast waves will be quantitatively discussed, as detailed numerical simulations are available in this case. This will be followed by a more qualitative discussion of the super-wind case.

2.2 The new supernova feedback prescription - theoretical considerations

2.2.1 Blast waves

To illustrate the effect of radiative cooling on the shocked region around a star-burst, it is first (incorrectly) assumed that all SNII energy is liberated at the same time, i.e. instantaneously in a small region. Furthermore, it is assumed that the ambient gas is homogeneously distributed, and that the release of explosion energy is isotropic. Initially, the radius of outward propagating shock-front is well described by the (adiabatic) Sedov-Taylor solution, viz.

$$R_{\text{ST}}(t) = \left(\frac{\xi E}{\rho_0} \right)^{1/5} t^{2/5}, \quad (2)$$

where E is the total energy released by the explosion, ρ_0 is the mass density of the surrounding gaseous medium; and $\xi = 2.026$ for an adiabatic index $\gamma = 5/3$ (Ostriker & McKee 1988). At about the time t_{sf} , the shock becomes radiative, and a cool dense shell is

formed behind the shock. An expression for this shell formation time is given by Cioffi, McKee & Bertschinger (1988) (CMB88):

$$t_{\text{sf}} = 3.61 \times 10^4 \frac{E_{51}^{3/14}}{\zeta_m^{5/14} n_0^{4/7}} \text{ yr}, \quad (3)$$

where n_0 is the ambient hydrogen number density in cm^{-3} , and E_{51} is the explosion energy in units of 10^{51} ergs. The radiative cooling function has been roughly approximated by $\Lambda = 1.6 \times 10^{-22} \zeta_m T_6^{-1/2} \text{ ergs cm}^3 \text{ s}^{-1}$, where $\zeta_m = 1$ corresponds to solar metallicity and T_6 is the temperature in units of 10^6 K .

At about t_{sf} the shocked region enters a new evolutionary stage that typically lasts for more than $10t_{\text{sf}}$: the pressure-driven snowplow (PDS) stage, in which the shell is driven outward by the pressure of the interior hot, dilute gaseous bubble - note though that due to radiative cooling and pressure effects, the mass of hot gas decreases during this stage, as will be discussed below. For $t_{\text{sf}} < t < 13t_{\text{sf}}$, CMB88 find that the radius of the shocked region is well approximated by an offset power law:

$$R_{\text{S}}(t) = R_{\text{PDS}} \left(\frac{4}{3} t_* - \frac{1}{3} \right)^{3/10}, \quad (4)$$

where $R_{\text{PDS}} = R_{\text{ST}}(t_{\text{PDS}} = t_{\text{sf}}/e)$ (e is the base of the natural logarithm) and $t_* = t/t_{\text{PDS}}$.

Subsequently, the PdV work done by the interior gaseous bubble on the outer, cool high-density shell becomes insignificant, and the shell expands at a slightly slower rate, as it enters the momentum conserving snowplow (MCS) phase, with the asymptotic behavior $R_{\text{S}} \propto t^{1/4}$ (Oort 1951), though CMB88 argue that in practice the exponent never reaches the asymptotic MCS value of 0.25. Finally, when the shock/shell speed becomes comparable to the sound speed of the ambient gaseous medium, the ambient pressure starts to affect the shock propagation, and the expansion stops. According to McKee & Ostriker (1977) this time can be expressed as

$$t_{\text{E}} = 10^{5.92} E_{51}^{0.31} n_0^{0.27} \tilde{P}_{04}^{-0.64} \text{ yr}, \quad (5)$$

where $\tilde{P}_{04} = 10^{-4} P_0 k^{-1}$, P_0 is the ambient pressure and k is Boltzmann's constant. CMB88 obtain a similar result for solar abundance — the abundance dependence is in any case very weak. The region continues to cool radiatively even after it stops expanding. McKee & Ostriker (1977) estimate that the time that the hot, low density interior will survive is approximately given by

$$t_{\text{max}} = 10^{6.85} E_{51}^{0.32} n_0^{0.34} \tilde{P}_{04}^{-0.70} \text{ yr}. \quad (6)$$

CMB88, and subsequently also Hellsten & Sommer-Larsen (1995), find the for $t_{\text{sf}} < t < 13t_{\text{sf}}$ the thermal energy of the hot, dilute gaseous interior decreases with time as

$$E_{\text{th}}(t) = 4.4 \times 10^{50} E_{51} \left(\frac{t}{t_{\text{sf}}} \right)^{-1.04} \text{ ergs}. \quad (7)$$

Hellsten & Sommer-Larsen (1995) showed, using the above expressions from CMB88, that the mass fraction of hot gas (defined as gas of $T > 10^5 \text{ K}$), for $t_{\text{sf}} < t < 13t_{\text{sf}}$ can be expressed as

$$\epsilon_{\text{hot}}(t) = \frac{T_0}{\bar{T}_{\text{hot}}} \left(\frac{t}{t_{\text{sf}}} \right)^{-1.94} n_0^{2/7} \zeta_m^{3/7} E_{51}^{1/7}, \quad (8)$$

where $T_0 = 9.2 \times 10^5 \text{ K}$, and \bar{T}_{hot} is the mean temperature of the hot gas. For the energies, densities and metallicities considered in this work, $\bar{T}_{\text{hot}} = 5 - 10 \times 10^5 \text{ K}$ - see Hellsten & Sommer-Larsen (1995) for details.

Due to the strong decrease of hot gas mass fraction with time,

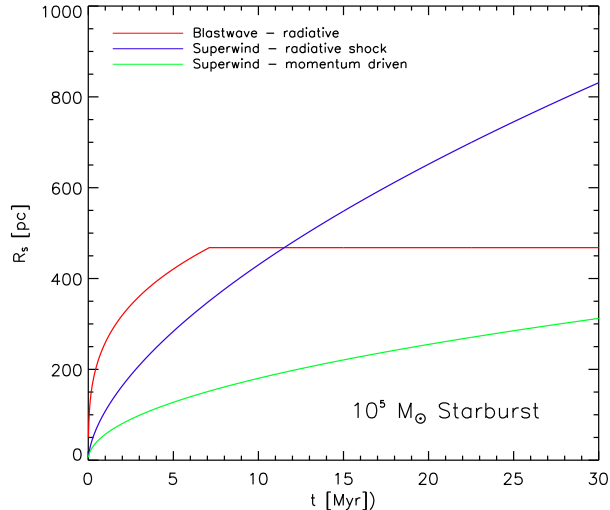


Figure 1. Evolution of blast wave and super wind outer shock radii with time, for a $M_* = 10^5 M_\odot$ “starburst”, and $n_0 = 1$. Red curve corresponds to a blast wave with effects of radiative cooling included, blue curve corresponds to a super-wind with a radiative shock and green curve corresponds to a momentum driven super-wind, such that effects of thermal pressure are neglected.

it is clear that only a minor fraction of the hot gas available at the time of shell formation is still hot when the shell stops expanding (eq. 5). As the hot interior continues cooling radiatively after $t = t_E$, an even smaller fraction of the “initial” hot gas survives hot till $t = t_{\text{SNII, end}} = 30.6$ Myr, which for the cases considered here is later than t_E . For continuity reasons alone, it is clear that the surviving hot gas must be located in the inner parts of the shocked region at $t \sim t_{\text{sf}}$ - this is also the region where the density is very small, and hence the cooling time very large — e.g., Landau & Lifshitz (1987).

To estimate the size of the region that survives as hot gas, we consider the specific case of a $M_* = 10^5 M_\odot$ “starburst”, exploding in gas of $n_0 = 1 \text{ cm}^{-3}$, and of solar abundance, i.e., $\zeta_m = 1$.

The number of stars of mass $M \geq 9 M_\odot$ (assumed to result in core-collapse supernovae) that are formed can be expressed as $N_{\text{SNII}} = \nu_{100} M_* / (100 M_\odot)$, where ν_{100} depends on the IMF adopted. For the Chabrier (2003) IMF, as implemented in this work, it is found that $\nu_{100} = 1.03$. Assuming that a total energy of 10^{51} ergs is deposited in the ambient gaseous medium per SNII, this results in $E_{51} = 1030$. From eq. (3) it follows that $t_{\text{sf}} = 1.6 \times 10^5$ yr, and from eq. (2) and the definition above that $R_{\text{PDS}} = 102$ pc — it has been assumed that $\rho_0 = 2.3 \times 10^{-24} n_0 \text{ g/cm}^3$, which is valid for solar abundance. From eq.(4) it follows that $R_{\text{sf}} \equiv R_S(t_{\text{sf}}) = 146$ pc, and the region will subsequently keep expanding until $t \simeq t_E = 7.1$ Myr ($\dot{P}_{04} = 1$ is adopted).

The analytical model of CMB88 indicates that their results can be extended to even later times than specified above, i.e., $t > 13 t_{\text{sf}}$. Hence, for the purposes of the order of magnitude estimates given in this work, we assume that eq.(4) describes the evolution of the blast wave/shell till $t = t_E = 7.1$ Myr ($\simeq 44 t_{\text{sf}}$). It follows that $R_E \equiv R_S(t_E) = 468$ pc — this will be somewhat of an overestimate, since the effect of the pressure of the ambient gas will be to reduce the expansion speed at $t \sim t_E$ - we comment on this below. It is, for simplicity, moreover assumed that $R_S(t > t_E) = R_E$ until $t = t_{\text{SNII, end}}$ (in reality the shell radius will initially oscillate

around the value given above, and eventually, as radiative cooling removes the pressure support from the interior, hot gas, start to implode at $t \sim t_{\text{max}} = 65$ Myr — e.g., McKee & Ostriker (1977)). The evolution of the blast wave shock radius with time, under the assumptions specified above, is shown in Fig. 1.

At $t = t_E$, the mass of the blast wave region will be $M_{bw}(t_E) \simeq \frac{4\pi}{3} R_E^3 \rho_0 = 1.5 \times 10^7 M_\odot$. This is somewhat of an overestimate, since R_E is overestimated — see above. Using eq.(8), it follows that an upper limit to the mass of hot gas at $t = t_E$ is $M_{\text{hot}} \simeq \epsilon_{\text{hot}}(t_E) M_{bw}(t_E) = 3.4 \times 10^4 M_\odot$ (a value of $\bar{T}_{\text{hot}} = 6.8 \times 10^5$ K has been adopted — this follows from the results and scaling relations given in Hellsten & Sommer-Larsen (1995)). At the time of shell formation, t_{sf} , the mass of the blast wave region is $M_{bw}(t_{\text{sf}}) \simeq \frac{4\pi}{3} R_{\text{sf}}^3 \rho_0 = 4.4 \times 10^5 M_\odot$. It follows that an upper limit to the fraction of gas at $t = t_{\text{sf}}$, that is still hot at $t = t_E$, is about $M_{\text{hot}}/M_{bw}(t_{\text{sf}}) = 0.077$. Moreover, at times later than t_E the thermal energy will continue decreasing — see above. Assuming, for lack of more detailed information, that the subsequent evolution of the thermal energy is described by $E_{\text{th}}(t) \propto t^{-1.04}$, (cf., eq.(7)), and that the mean temperature of the hot gas is approximately constant, it follows that, at $t = t_{\text{SNII, end}}$, $M_{\text{hot}} \simeq 7.4 \times 10^3 M_\odot \simeq 0.017 M_{bw}(t_{\text{sf}})$. So, only a few percent of the gas available at the time of onset of shell formation remains hot till $t = t_{\text{SNII, end}}$. Approximating the gas distribution at $t = t_{\text{sf}}$ by the Sedov-Taylor profile for adiabatic index $\gamma = 5/3$ (see, e.g., Landau & Lifshitz (1987) for details), it can be shown that only the gas situated inside of $0.6 R_{\text{sf}}$ remains hot till $t = t_{\text{SNII, end}}$.

So, as a consequence of the arguments given above, it seems reasonable to only switch radiative cooling off for SPH particles located inside some fraction (denoted β in the following) of $R_S(t)$.

2.2.2 Star-burst driven super winds

In reality, simultaneously formed massive stars of different masses do not explode as SNIIs at the same time. The most massive O stars considered in this work, of mass $100 M_\odot$, explode after about $t_{60} = 3.4$ Myr, whereas the least massive stars that explode as SNIIs, assumed here to be B stars of mass $9 M_\odot$, explode after about $t_8 = 34$ Myr. For standard IMFs (note that the Chabrier (2003) and Salpeter (1955) IMFs have very similar slopes at the high mass end), the resulting SNII luminosity is approximately constant during the time interval $t_{60} \leq t \leq t_8$ (see, e.g., McCray & Kafatos (1987)), so for simplicity, the luminosity will be assumed to be constant in the following.

For an adiabatic super wind, the evolution of the shock radius is given by

$$R_{\text{SW}}(t) = \alpha \left(\frac{L_{\text{SW}}}{\rho_0} \right)^{1/5} t^{3/5}, \quad (9)$$

where $L_{\text{SW}} = \dot{E}_{\text{SNII}}$ is the luminosity of the star burst, and $\alpha = 0.88$ (e.g., Weaver et al. 1977). After a relatively short time, the shock becomes radiative. This time can be expressed as

$$t_{\text{cool}} = 3.4 \times 10^4 \left(\frac{L_{\text{SW},39}}{n_0} \right)^{1/2} \text{ yr}, \quad (10)$$

where $L_{\text{SW},39}$ is the luminosity in units of 10^{39} ergs/sec (Castor et al. 1975) Subsequently, as long as radiative cooling of the hot interior is not important, the evolution of the shock radius

is given approximately by

$$R_{\text{SW}}(t) = \alpha \left(\frac{L_{\text{SW}}}{\rho_0} \right)^{1/5} t^{3/5} = 105 \left(\frac{L_{\text{SW},39}}{n_0} \right)^{1/5} t_6^{3/5} \text{ kpc} , \quad (11)$$

where $\alpha = 0.76$ has been assumed (e.g., Weaver et al. 1977), and t_6 is the time in Myrs. Given that the adiabatic phase is so brief, eq.(11) will be used in the following to express the evolution of the super-wind shock radius. During the radiative shock phase, the thermal energy of the super-wind region is given by $\frac{5}{11} L_{\text{SW}} t$, i.e., at any time about 45% of the total amount of super-nova energy released.

At some point in time, radiative cooling of the interior will start to affect the expansion of the super-wind. Expressions for the temporal evolution of the thermal energy, like eq. (7) and (8) above, are unfortunately not available in the literature. However, one can estimate the evolution of the shock radius with time, in the case of complete radiative cooling, as follows:

In general, under simplifying conditions, the time derivative of total (radially outward directed) momentum of the super-wind region can be expressed as

$$\frac{d}{dt} M \bar{v} \simeq 4\pi R_{\text{SW}}^2 \bar{p} + \dot{M}_{\text{SB}} v_{\text{SB}} , \quad (12)$$

where M is the total mass of the super-wind region, \bar{v} is the mass averaged radial velocity, \bar{p} is the volume averaged pressure, \dot{M}_{SB} is the rate of mass ejection by the central star-burst and v_{SB} is the average mass ejection velocity, assumed to be constant. $\dot{M}_{\text{SB}} v_{\text{SB}}$ is the momentum injection rate in the central star-burst region. The main assumptions made are 1) that the shock is strong, and 2) that the region of momentum injection is much smaller than R_{SW} . In the case where the average pressure can be neglected, due to effects of radiative cooling, eq. (12) simplifies to

$$\frac{d}{dt} M \bar{v} \simeq \dot{M}_{\text{SB}} v_{\text{SB}} = \frac{2\eta L_{\text{SW}}}{v_{\text{SB}}} , \quad (13)$$

where η is fraction of total star-burst energy, that comes out in the form of kinetic energy. For the Sedov-Taylor solution, $\eta \simeq 0.28$. As most of the swept-up mass is concentrated in a thin shell behind the outer shock, $\bar{v} \simeq v_{\text{SW}}$, where v_{SW} is the shock speed. Hence, eq. (13) can be integrated to yield

$$R_{\text{SW,kin}}(t) \simeq \left(\frac{3\eta L_{\text{SW}}}{\pi \rho_0 v_{\text{SB}}} \right)^{1/4} t^{1/2} . \quad (14)$$

Inserting characteristic values yields

$$R_{\text{SW,kin}}(t) \simeq 45 \left(\frac{\eta_{0.28} L_{\text{SW},39}}{n_0 v_{\text{SB},3000}} \right)^{1/4} t_6^{1/2} \text{ pc} , \quad (15)$$

where $\eta_{0.28} = \eta/0.28$ and $v_{\text{SB},3000} = v_{\text{SB}}/3000$ km/s. For typical values, $L_{\text{SW},39} \sim 1$ (see below) and $v_{\text{SB},3000} \sim 1$ (from supernova energetics), $R_{\text{SW,kin}}/R_{\text{SW}} \lesssim 0.5$ for $t \gtrsim 0.2$ Myr.

To be specific, we again consider the case of a $M_* = 10^5 M_\odot$ star-burst, located in ambient gas of $n_0 = 1 \text{ cm}^{-3}$. Assuming constant luminosity, the luminosity will be given by

$$L_{\text{SW}} = \left(\frac{\nu_{100} M_* E_{\text{SN}}}{(100 M_\odot) t_{\text{SNII,end}}} \right) = 1.07 \times 10^{39} \left(\frac{M_*}{10^5 M_\odot} \right) \text{ erg/sec} , \quad (16)$$

where E_{SN} is the thermal plus kinetic energy release by one supernova, again assumed to be 10^{51} ergs. Hence, $L_{\text{SW},39} = 1.07$. Inserting this, and $n_0 = 1$ in eq.(11), results in the blue curve shown in Fig. 1. When the shock speed eventually becomes comparable to the sound speed of the ambient gaseous medium, the ambient pressure starts to affect the shock propagation, halting the expansion.

As can be seen from the figure, this happens at a somewhat later time, than for the blast wave (comparing the slope of the red curve at $t = t_E$ to the slope of the blue curve at any t), so, for simplicity, this has not been incorporated in the figure. Also shown in the figure, by the green curve, is the momentum-driven case, where the effect of the pressure of the interior is neglected. The shock speed becomes comparable to the sound speed after a few Myr, so at later times, the green curve is a conservative upper limit to the actual radius of the super-wind region for this (albeit extreme) case.

Lacking detailed numerical simulations, we can only state that it quite likely that the actual radius of the super-wind region, $R_{\text{SW}}(t)$, is somewhat less than the expression given above by eq.(11). The radius, within which the hot gas does not cool radiatively during the entire supernova feedback period, $t_{\text{SNII,end}}$, is obviously even less than this. So, as for the blast wave case, it seems reasonable to only switch radiative cooling off for SPH particles located inside some fraction, β , of $R_{\text{SW}}(t)$ (eq. 11).

2.2.3 Super wind breakthrough and breakout from the disk

At present, the thin, dense part of the Galactic disk has a scale height of about 200 pc (e.g., Heiles 1990). When the radius of the super wind becomes comparable to this scale height, the super wind will start moving in directions perpendicular to the disk (e.g., Koo & McKee 1992; Mac Low & Ferrara 1999), and “break-through” has occurred. According to Koo & McKee (1992) this occurs if the star-burst results in at least ~ 50 SNII’s. If the burst results in at least ~ 1000 SNII’s, the vertically moving super wind will move through the much more extended (scale height ~ 1 kpc), but lower density ($n_0 \sim 0.05 \text{ cm}^{-3}$) HII layer as well, and complete “breakout” occurs, in which significant amounts of shocked gas completely leaves the galaxy (Koo & McKee 1992).

2.3 The new supernova feedback prescription - implementation

As discussed in sections 2.2.1-2.2.3, a $M_* = 10^5 M_\odot$ star burst, results in about 1000 SNII’s, and hence super wind breakout is likely to occur. As shown by the above authors, when the super wind radius reaches about the scale height of the disk, the geometry of the super wind will change from spherical to approximately that of a bi-polar outflow, perpendicular to the plane of the disk. As can be seen from Fig. 1, $R_{\text{SW}} \sim 200$ pc already at $t \sim 3$ Myr for the radiative shock super wind, in cases where a cold gaseous disk has been established. Hence, after that time it would be incorrect to switch radiative cooling off for all SPH particles inside of $R_{\text{SW}}(t)$, as some of these particles will never be affected by the super wind. As can be seen from the Figure, at $t \sim t_{\text{SNII,end}}$ $R_{\text{SW}} \sim 800$ pc for the spherically symmetric radiative shock super wind. Motivated by this, and the arguments given above, radiative cooling is, at any given time t , only switched off for SPH particles located inside of $\beta R_{\text{SW}}(t)$ (eq. 11), where $\beta = 0.25$ is adopted.

The energy and momentum feedback from the star burst is of course deposited in the small region containing the newborn massive stars. This region will in general be considerably smaller than the scale height of the disk, so one should in principle, at least at late times, deposit the energy to even fewer SPH particles than the ones for which radiative cooling is switched off. Following Stinson et. al (2006), however, we choose to feed star burst energy to all particles, for which cooling has been turned off — extensive testing indicates that it makes no significant difference to the results. We

furthermore require that at least $N_{\text{SPH},\text{min}} = 2$ SPH particles have radiative cooling switched off and receive SNII energy feedback — variations of $N_{\text{SPH},\text{min}}$ by a factor of two makes no significant difference to the results either. We note that, since the SPH implementation is based on solving the entropy equation, even injecting all energy into one particle only, still gives approximately the correct behavior of an explosion — see Springel & Hernquist (2002) for details.

2.4 Early stellar feedback

Thermal supernova feedback alone, even when implemented as described above, is not sufficient to completely prevent “over-cooling”, at least when it is assumed that each SNII releases at most 10^{51} erg. This results in galaxies with too massive central concentrations of stars, leading in turn to too centrally peaked rotation curves (e.g., Stinson et al. 2010; Scannapieco et al. 2012).

Moreover, recently, abundance matching techniques (Conroy et al. 2006) have been used to compare total halo masses with galaxy stellar masses (Conroy & Wechsler 2009; Moster et al. 2010; Guo et al. 2010; Behroozi et al. 2010; Moster et al. 2013). Guo et al. (2010) and Sawala et al. (2011) showed that most galaxy formation simulations form too many stars compared to what abundance matching predicts.

Even without over-cooling, van den Bosch et al. (2002) showed that the amount of low angular momentum material in collapsed collision-less halos exceeds the amount of low angular momentum material observed in disk galaxies. Consequently, this low angular momentum material needs to be removed from the center of the system.

During the first 3.4 Myr after a population of stars has been formed, the massive stars emit large amounts of (primarily UV) radiation, but no SNII explosions are taking place. This early stellar feedback (ESF) can modify the ISM around the stellar population, effectively suppressing star formation in a region around the new born stars. Indeed, Murray et al. (2010) showed that there can be significant feedback effects from stars before they explode as supernovae. Moreover, Hopkins et al. (2011) incorporated a kinetic radiation pressure feedback into simulations of isolated disk galaxies and found that the feedback could strongly regulate star formation.

Motivated by this, Stinson et. al (2013) implemented a scheme based on thermal pressure to provide feedback during the time between when stars are formed and the first SNs explode — see also Wang et al (2015). Using this early stellar feedback (ESF) prescription, Macciò et al. (2012) showed that the feedback removes low angular momentum dark matter in galaxies up to nearly L^* , producing cored dark matter density profiles. Stinson et al. (2012) showed that the metal rich outflows created by this feedback match observations of OVI in the circum-galactic medium of star forming galaxies. Brook et al. (2012a,b) also showed that a sample of galaxies, of masses less than or similar to that of the Milky Way, form disks that follow a wide range of disk scaling relationships.

The radiation feedback from massive stars has been implemented in the code following Stinson et. al (2013): To model the luminosity of stars, a simple fit of the mass-luminosity relationship observed in binary star systems by Torres (2010) is used:

$$\frac{L}{L_{\odot}} = \begin{cases} \left(\frac{M}{M_{\odot}}\right)^4, & M < 10M_{\odot} \\ 100\left(\frac{M}{M_{\odot}}\right)^2, & M > 10M_{\odot} \end{cases} \quad (17)$$

This relationship leads to about 3×10^{50} ergs of energy being re-

leased from the high mass stars per M_{\odot} of the entire stellar population over the 3.4 Myr between the formation of the stellar population and the commencing of SNII. These photons do not couple efficiently with the surrounding ISM (Freyer et al. 2006), so only a fraction, ϵ_{ESF} (of the order 10% — see further below), of the radiation energy is injected as thermal energy in the surrounding gas. Moreover, radiative cooling is not turned off for this form of energy input. It is well established that such thermal energy injection is highly inefficient at the spatial and temporal resolution of the type of cosmological simulations used here (Katz 1992; Kay et al. 2002). Though the dynamical effect is limited, ESF effectively halts star formation in the region immediately surrounding a recently formed stellar population by increasing the temperature above the threshold temperature for star formation. We note that Hopkins et al. (2014) also find that the non-linear interaction of ESF and supernova feedback is critical to explain large-scale outflows, self-regulation of star formation etc.

2.5 The simulations

The basis for the hydro/gravity simulations was a cosmological, dark matter (DM) only simulation of a “field-galaxy” region. The cosmological initial conditions were based on a Λ CDM model with $(\Omega_M, \Omega_{\Lambda})=(0.3,0.7)$ and a Hubble parameter $H_0 = 100h \text{ km s}^{-1} \text{ Mpc}^{-1} = 65 \text{ km s}^{-1} \text{ Mpc}^{-1}$, close to the parameters suggested by the most recent Planck 2015 results. The simulation had co-moving box length $10 h^{-1} \text{ Mpc}$, and was evolved from a starting redshift of $z_i = 39$ to $z = 0$ assuming periodic boundary conditions — more detail on the DM only simulation is given in Sommer-Larsen, Götz & Portinari (2003). At $z = 0$, the 20 most massive haloes (see further below) were selected — they span a range of virial masses of $M_{\text{vir}} \sim 6 \times 10^{11} - 4 \times 10^{12} M_{\odot}$. Mass and force resolution was increased in Lagrangian regions enclosing the haloes, and in these regions all DM particles were split into a DM particle and a gas (SPH) particle according to an adopted universal baryon fraction of $f_b=0.15$, in line with recent estimates. The evolution of these regions was then re-simulated using hydro/gravity code described in section 2 — this approach has been dubbed the “zoom-in” technique — full detail is given in Sommer-Larsen, Götz & Portinari (2003). Particle masses were $m_{\text{SPH}}=m_{*}=7.3 \times 10^5$ and $m_{\text{DM}}=4.2 \times 10^6 h^{-1} M_{\odot}$, and gravity spline softening lengths (approximately force resolution) were $\epsilon_{\text{SPH}}=\epsilon_{*}=380$ and $\epsilon_{\text{DM}}=680 h^{-1} \text{ pc}$. The number of SPH+DM particles per re-simulated halo region lies in the range $2.5 \times 10^5 - 1.5 \times 10^6$ for these medium-resolution simulations. The ESF efficiency was set to $\epsilon_{\text{ESF}}=0.10$ for these runs — see below.

The simulations were evolved from a starting redshift of $z_i = 39$ to $z = 2.58$. At $z = 2.58$ the 20 simulations contain a total of 158 well resolved primary haloes (i.e., not counting sub-haloes) of virial masses $M_{\text{vir}} \sim 10^{10} - 10^{12} M_{\odot}$. The stellar masses of the corresponding primary galaxies span the range $M_{*} \sim 10^7 - 10^{10} M_{\odot}$.

In addition to the above 20 re-simulations, another 20 re-simulations of scaled-up versions of the regions were undertaken. Linear scales and velocities were scaled by a factor 1.6, masses were correspondingly scaled by a factor $1.6^3 \simeq 4.1$. Since the Λ CDM power-spectrum is fairly constant over this limited mass range, the rescaling is a reasonable approximation. The reason why such more massive haloes are also re-simulated is that massive galaxies are crucial for the purposes of this paper, as will be detailed in the following. Particle masses were $m_{\text{SPH}}=m_{*}=3.0 \times 10^6$ and $m_{\text{DM}}=1.7 \times 10^7 h^{-1} M_{\odot}$, and gravity spline softening

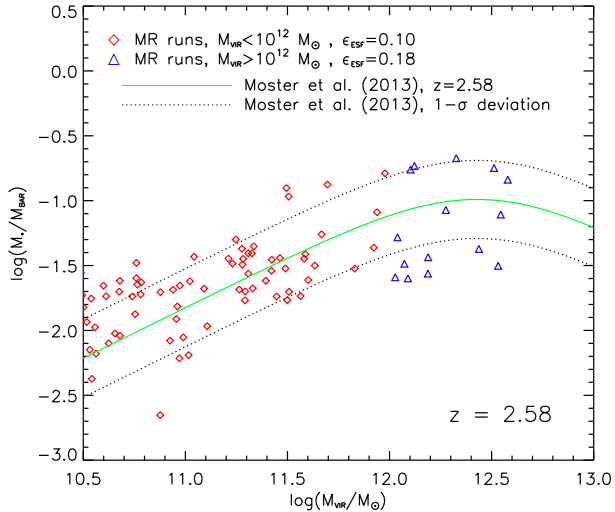


Figure 2. M_*/M_{bar} vs. M_{vir} relation at $z=2.58$ for the medium resolution runs. Most galaxies have been run with $\epsilon_{ESF}=0.10$, but galaxies of $M_{vir} > 10^{12} M_\odot$ have been run with $\epsilon_{ESF}=0.18$. Also shown is the Moster et al. (2013) relation for $z=2.58$, together with the $1-\sigma$ deviation curves, also from Moster et al. (2013).

lengths (approximately force resolution) were $\epsilon_{SPH}=\epsilon_*=610$ and $\epsilon_{DM}=1090 h^{-1}pc$. The ESF efficiency was set to $\epsilon_{ESF}=0.18$ for these runs — see below. At $z = 2.58$ the 20 simulations of the scaled regions contain a total of 20 well resolved primary haloes of virial masses $M_{vir} \sim 10^{12} - 4 \times 10^{12} M_\odot$ — only haloes of $M_{vir} \geq 10^{12} M_\odot$ are considered in the analysis of the scaled regions. The stellar masses of the corresponding primary galaxies span the range $M_* \sim 10^{10} - 10^{11} M_\odot$.

The ESF efficiencies were chosen such that, at $z=2.58$, the ratio between the galaxy stellar mass and the total baryonic mass available inside of the virial radius, M_*/M_{bar} , as a function of virial mass approximately follows the relation suggested by Moster et al. (2013) (for $z=2.58$). For the scaled-up runs, a few galaxies of $M_*/M_{bar} < 0.02$ were omitted from the analysis — this does not affect the analysis in any way. The resulting M_*/M_{bar} vs. M_{vir} relation at $z=2.58$ is shown in Fig. 2.

Subsequently, for the actual production runs, the 40 simulations were redone at four times higher mass resolution and 1.6 times higher force resolution. For the unscaled haloes, these HR simulations had particle masses of $m_{SPH}=m_*=1.8 \times 10^5$ and $m_{DM}=1.1 \times 10^6 h^{-1} M_\odot$, and gravity spline softening lengths were $\epsilon_{SPH}=\epsilon_*=240$ and $\epsilon_{DM}=430 h^{-1}pc$. For the scaled-up versions, the corresponding values are $m_{SPH}=m_*=7.4 \times 10^5$ and $m_{DM}=4.5 \times 10^6 h^{-1} M_\odot$, $\epsilon_{SPH}=\epsilon_*=380$ and $\epsilon_{DM}=680 h^{-1}pc$.

The number of SPH+DM particles per re-simulated HR halo region was about $1-6 \times 10^6$. As found by Stinson et. al (2013), when the numerical resolution is increased, the ESF efficiency typically has to be decreased slightly, to result in a HR stellar galaxy of the same mass as the corresponding MR stellar galaxy. For the HR simulations of $M_{vir} \leq 10^{12} M_\odot$ haloes, values of $\epsilon_{ESF}=0.08-0.09$ were used. For the $M_{vir} > 10^{12} M_\odot$ haloes, $\epsilon_{ESF}=0.15-0.16$.

In order to increase the number of lower mass galaxies, data for 27 HR simulations, aimed at producing disk galaxies at $z=0$ of stellar masses comparable to that of the Milky Way or less, were included in the analysis. The simulations are characterized by $m_{SPH}=m_*=0.9-2.8 \times 10^5$ and $m_{DM}=0.5-1.6 \times 10^6 h^{-1} M_\odot$,

and gravity spline softening lengths were $\epsilon_{SPH}=\epsilon_*=190-280$ and $\epsilon_{DM}=340-490 h^{-1}pc$. For these simulations, SPH+DM particle numbers are $1-3 \times 10^6$. At $z = 2.58$ the 27 simulations contain a total of 65 well resolved primary haloes of virial masses $M_{vir} \sim 0.3-6 \times 10^{11} M_\odot$. The stellar masses of the corresponding primary galaxies span the range $M_* \sim 10^8 - 3 \times 10^9 M_\odot$.

It turns out, that the results obtained in this paper are quite insensitive to whether this additional sample of HR disk galaxy simulations is included or not. However, to improve the statistics and the resolution at lower galaxy masses, we chose to include it in the following.

3 RESULTS AND ANALYSIS

3.1 SII column densities

At $z=2.58$, all galaxies located in the 2×20 haloes simulated, as well as in the HR disk galaxy simulations, are analyzed, subject to a SFR selection criterion: only galaxies of SFR above a threshold SFR_{detect} are considered as being potential DLA galaxies — this is in order to mimic the observational situation. For most purposes, we adopt $\log(SFR_{detect}) = -0.5$ (where the SFR is expressed in M_\odot/yr), but we shall also consider other values of SFR_{detect} . It turns out, that the main results obtained are quite insensitive to the choice of this parameter. As will be shown below, $\log(SFR_{detect}) = -0.5$ corresponds to $M_V \simeq -18.5$, 4-5 magnitudes fainter than (the observational) $M_{V,*}$ at such redshifts. With the above selection criterion, a total of 95 galaxies are selected at $z=2.58$.

We shall in this work focus on calculating the column density of singly ionized Sulfur. The reason for this is threefold: a) Sulfur is only weakly depleted on to dust grains (e.g., Fitzpatrick & Spitzer (1997), but see also Calura et al. (2009), and Jenkins (2009)), b) the abundance of S is tracked in the simulations, and c) N(SII) is determined very accurately for the DLA: Fynbo et al. (2011) obtain $\log(N(SII)) = 15.82 \pm 0.01$.

For each galaxy selected, 600 sight-lines were shot through the galaxy at random positions and directions, though constrained such that, for every sight-line, the impact parameter was 16.2 kpc. Along each sight-line, the column density of Sulfur II, $N(SII)$, is calculated over a 1000 kpc path, centered at the galaxy, viz.

$$N(SII) = \int_{-l_{max}}^{l_{max}} n_{SII}(l) dl, \quad (18)$$

where $n_{SII}(l)$ is the number density of Sulfur II as a function of the position along the line-of-sight, and $l_{max} = 500$ kpc (below we discuss the contribution from non-local SII). At a given position, the fraction of singly ionized Sulfur atoms, f_{SII} , depends on the local hydrogen density, n_H , temperature, T , radiation intensity, $J(\nu)$ (where ν denotes frequency), and also (though weakly), on the gas metal abundance. This allows eq. (18) to be rewritten as

$$N(SII) = \int_{-l_{max}}^{l_{max}} n_S(\mathbf{x}) f_{SII}(n_H(\mathbf{x}), T(\mathbf{x}); J(\nu, \mathbf{x})) dl, \quad (19)$$

where \mathbf{x} denotes the position corresponding to line-of-sight length l , and the weak dependence on metal abundance has been neglected. Adopting the mean field approximation of Rahmati et al. (2013) it is assumed that the local radiation field depends mainly on the local hydrogen number density $n_H(\mathbf{x})$. The radiation field is modeled as a superposition of a transmitted UVB part and a (hydrogen) recombination radiation part. At a given redshift z , it is assumed that a fraction, f_{RR} , of the local photo-ionization rate is

due to recombination radiation and that the remaining fraction of the photo-ionization, $f_{\text{TR}} = (1.0 - f_{\text{RR}})$, is caused by transmitted UVB radiation. The fractions f_{RR} and f_{TR} are assumed to be functions of n_H and z , and are modeled in accordance with the results of Rahmati et al. (2013) — generally, at low n_H , transmitted UVB dominates, and, at large n_H , recombination radiation dominates. Finally, based on n_H , T and the local radiation field, f_{SII} is determined at the position of each SPH particle using CLOUDY (Ferland et al. 2013) — more detail will be given in a forthcoming paper.

In practice, eq. (19) is discretized as

$$N(\text{SII}) \approx \sum_{i=-N_{\text{max}}}^{N_{\text{max}}} n_S(\mathbf{x}_i) f_{\text{SII}}(n_H(\mathbf{x}_i), T(\mathbf{x}_i); J(\nu, \mathbf{x}_i)) \Delta l, \quad (20)$$

where $N_{\text{max}}=5000$ was adopted, implying $\Delta l = l_{\text{max}}/N_{\text{max}} = 0.1$ kpc — this choice of Δl was found to give stable results in the discretisation. At each point in space, \mathbf{x}_i , the number density of Sulfur II is estimated using the cubic spline smoothing kernel of Monaghan & Lattanzio (1985), as

$$n_{\text{SII}}(\mathbf{x}_i) = \frac{\rho_{\text{SII}}(\mathbf{x}_i)}{m_S} = \frac{1}{m_S} \sum_{j=1}^{N_n} m_j Z_S(\mathbf{x}_j) f_{\text{SII}}(n_H(\mathbf{x}_j), T(\mathbf{x}_j); J(\nu, \mathbf{x}_j)) W(x_{ij}, h_i), \quad (21)$$

where m_S is the mass of a Sulfur atom, m_j is the mass of SPH particle j (all SPH particles have the same mass in the present study), $Z_S(\mathbf{x}_j)$ is the Sulfur abundance (by mass) of SPH particle j , $x_{ij} = |\mathbf{x}_j - \mathbf{x}_i|$, W is the smoothing kernel, N_n is the number of SPH neighbors in the SPH formalism ($N_n=50$ in the present simulations), and h_i is chosen such that if the SPH particles are ordered after increasing distance to \mathbf{x}_i , then $2h_i$ corresponds to the distance halfway between particle N_n and particle $N_n + 1$. Hence, eq. (20) is finally expressed as

$$N(\text{SII}) \approx \frac{1}{m_S} \times \sum_{i=-N_{\text{max}}}^{N_{\text{max}}} \left[\sum_{j=1}^{N_n} m_j Z_S(\mathbf{x}_j) f_{\text{SII}}(n_H(\mathbf{x}_j), T(\mathbf{x}_j); J(\nu, \mathbf{x}_j)) W(x_{ij}, h_i) \right] \Delta l. \quad (22)$$

A sight-line through a given galaxy (1) at impact parameter $b = 16.2$ kpc is counted if there is not another galaxy (2), of $\text{SFR}_2 > \text{SFR}_{\text{detect}}$ and $\text{SFR}_2 \geq \text{SFR}_1$, situated such that the impact parameter of the sight-line is less than 16.2 kpc relative to that galaxy (if the impact parameter of the second galaxy is less than 3 kpc it is assumed that the second galaxy is undetected due to the brightness of the QSO, so the sight-line is counted, unless a third galaxy full fills the conditions above).

For each galaxy, the fraction of the number of sight-lines with $\log(N(\text{SII})) \geq 15.82$ relative to the total number of “permitted” (see above) sight-lines, $p_{15.82}$ is determined. $p_{15.82}$ can be interpreted as the probability of finding $\log(N(\text{SII})) \geq 15.82$ at $b = 16.2$ kpc for a particular galaxy. Subsequently, for the 95 galaxies, the $p_{15.82}$ ’s are binned according to M_V , for M_V in the range $[-18; -25]$ with a bin size of 1 mag.. For $M_V > -18$, no galaxies were found to display $\log(N(\text{SII})) \geq 15.82$, and none of the simulated galaxies had $M_V < -25$. In this way, seven probabilities, $f_{15.82}(M_V)$, are

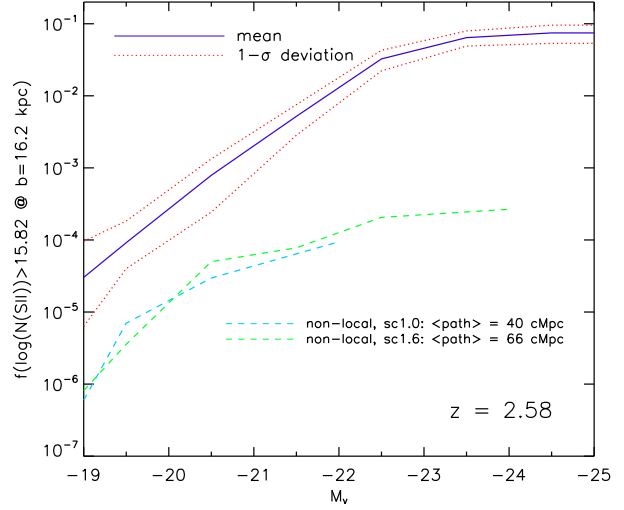


Figure 3. Probability of finding $\log(N(\text{SII})) \geq 15.82$ for a sight-line at impact parameter $b = 16.2$ kpc relative to a given galaxy of absolute magnitude M_V at $z=2.58$. The mean value is shown by the blue line, and the $1-\sigma$ (statistical) range is indicated by the dotted red lines. Also shown, by the magenta and green dashed lines, are the probabilities that the SII absorption is caused by non-local galaxies of physical distances of $0.2 < d < 11$ Mpc and $0.2 < d < 18$ Mpc, respectively. This corresponds to velocity shifts of up to 3000 and 4800 km/s, respectively, for a pure Hubble flow — see subsection 4.2 for more detail.

obtained — these are displayed in Fig. 3 together with the statistical $1-\sigma$ deviations. As can be seen from the figure, for galaxies of $M_V \lesssim M_V^*$ (~ -23 , see below), of order 10% of the sight-lines through the galaxies at impact parameter $b=16.2$ kpc will display a Sulfur II column density of $N(\text{SII}) \geq 10^{15.82} \text{ cm}^{-2}$ (the value observed for the DLA) — this is one of the main results of this paper.

The line-of-sight extent or “thickness” of the SII distribution can be roughly estimated as two times the dispersion of the SII number density weighted position along the los. Denoting

$$\bar{l}^2 = \int_{-l_{\text{max}}}^{l_{\text{max}}} l^2 \cdot n_{\text{SII}}(l) dl, \quad (23)$$

and

$$\bar{l} = \int_{-l_{\text{max}}}^{l_{\text{max}}} l \cdot n_{\text{SII}}(l) dl, \quad (24)$$

the los position dispersion is calculated as

$$\sigma_l = \sqrt{\bar{l}^2 - \bar{l}^2}. \quad (25)$$

For lines-of-sight of $\log(N(\text{SII})) \geq 15.82$, typical values of the order $\sigma_l \sim 10$ kpc are found. Hence the thickness of the SII “layer” is of the order 20 kpc, but with a considerable variation.

3.2 Models of the $z=2.58$ galaxy luminosity function

As shown in the previous subsection, the probability of finding near-solar metallicity at an impact parameter of $b = 16.2$ kpc (not surprisingly) increases with galaxy luminosity. On the other hand, it is well known that the number density of galaxies per unit luminosity as a function of luminosity, $dN(L)/dL$, decreases with luminosity, especially at $L \gtrsim L_*$, where the decrease is approximately

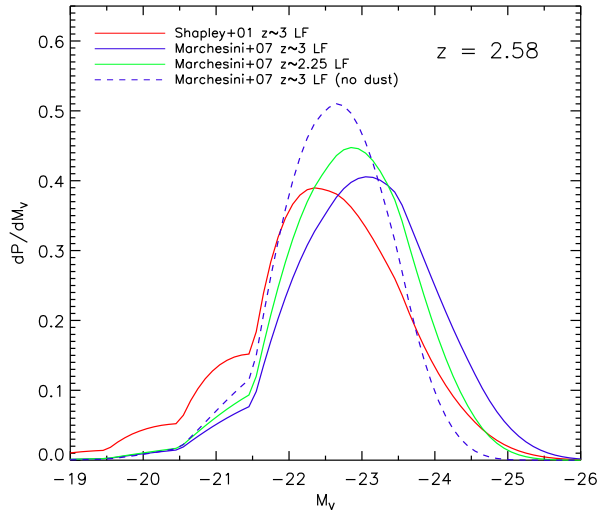


Figure 4. Probability distributions, $P(M_V)$, for the three different extinction corrected LFs (S01: red curve, M07 $z\sim 3$: blue, solid curve, M07 $z\sim 2.25$: green curve). Also shown is the $P(M_V)$ resulting from not extinction correcting the M07 $z\sim 3$ LF (blue, dashed curve).

exponential. To determine the (Bayesian) probability distribution of finding $\log(N(\text{SII})) \geq 15.82$ at $b = 16.2$ kpc as a function of M_V or SFR , one has to fold the two distributions:

Since no luminosity functions (LFs) at $z=2.58$ are available, we shall consider three different observational models of the LF, spanning a redshift range of $\sim 2.25-3$ and a wide range of faint end slopes. The first is the $z\sim 3$ V-band (rest-frame) LF of Shapley et al. (2001) (S01), the second is the $z\sim 3$ V-band (rest-frame) LF of Marchesini et al. (2007) (M07 $z\sim 3$) and the third the $z\sim 2.25$ R-band (rest-frame) LF of Marchesini et al. (2007) (M07 $z\sim 2.25$).

As is well known, even at $z \sim 3$, effects of dust extinction on the luminosities of galaxies are considerable (e.g., Sommer-Larsen & Fynbo 2008). As the quantities described in the previous subsection, such as $p_{15.82}(M_V)$ depend on true luminosities etc., it is consequently important to correct the observed luminosity functions for effects of dust extinction. Details about the luminosity functions and how the extinction corrections are performed are given in the appendix of this paper, and the reader is referred to the appendix for all such detail.

3.3 The constrained probability functions

The aim in this section is the following: given that a DLA of $\log(N(\text{SII})) \geq 15.82$ is located at impact parameter $b=16.2$ kpc relative to a galaxy, what typical values of M_V and $\log(SFR)$ would the galaxy then be expected to have, based on the galaxy formation simulations presented in this paper?

To be quantitative, we calculate the (Bayesian) probability distributions of M_V and $\log(SFR)$ as follows: For a given small galaxy luminosity interval $[L_V, L_V + dL_V]$, the probability per unit volume, dP , of finding $\log(N(\text{SII})) \geq 15.82$ at impact parameter $b=16.2$ kpc relative to a galaxy must be proportional to

$$\frac{dN_{corr}}{dL_V}(L_V) f_{15.82}(L_V) dL_V, \quad (26)$$

where $f_{15.82}$ was determined in subsection (3.1). Changing vari-

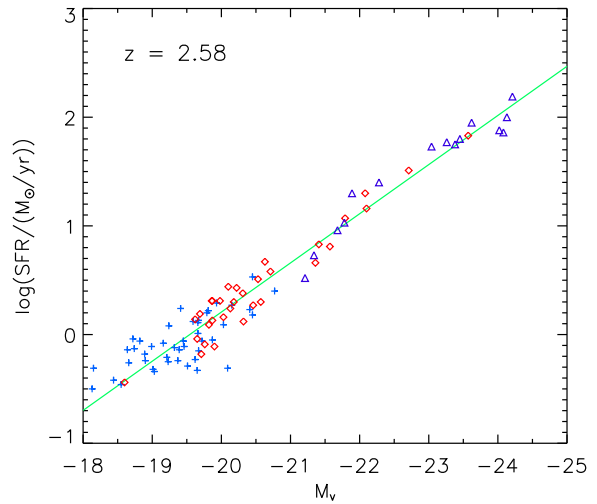


Figure 5. Relation between $\log(SFR)$ and M_V for the simulated galaxies at $z=2.58$. The rescaled HR halo simulations are shown by dark blue triangles (15 galaxies), the unscaled HR simulations by red squares (32 galaxies) and the HR disk galaxy simulations by light blue crosses (48 galaxies). Also shown is a linear regression fit to the data.

able from L_V to M_V , we obtain

$$dP \propto \frac{dN_{corr}}{dL_V} \cdot \frac{dL_V}{dM_V} f_{15.82}(M_V) dM_V = -\frac{L_V}{2.5 \log(e)} \cdot \frac{dN_{corr}}{dL_V} f_{15.82}(M_V) dM_V. \quad (27)$$

Consequently, under the constraining condition that only $b=16.2$ kpc sight-lines of $\log(N(\text{SII})) \geq 15.82$ are considered, the probability distribution of DLA galaxy M_V is given by

$$\frac{dP}{dM_V} = \frac{\frac{dN_{corr}}{dL_V} f_{15.82}(M_V) L_V(M_V)}{\int_{-\infty}^{\infty} \frac{dN_{corr}}{dL_V} f_{15.82}(M'_V) L_V(M'_V) dM'_V}. \quad (28)$$

In Fig. 4 the resulting probability distributions are shown for the three different extinction corrected LFs. To illustrate the effect of the extinction correction, the probability distribution resulting from not extinction correcting the M07 $z\sim 3$ LF is also shown. It is seen, that the probability distributions peak at $L \sim L^*$, which is another main result of this work. It is also seen that for the S01 LF, the probability distribution is skewed somewhat towards lower luminosities, due to the steep faint end slope of the S01 LF. For comparison to observations, it is also convenient to express the probability functions as functions of galaxy SFR. In Fig. 5 the relation between SFR and M_V is shown for the 95 HR sample galaxies. It is seen, that there is a quite tight relation between the two quantities. By linear regression one obtains

$$\log(SFR) = -0.452M_V - 8.84, \quad (29)$$

where SFR is expressed in units of M_\odot/yr . This corresponds to $SFR \propto L_V^{1.13}$, so the two quantities are approximately linearly related over the range of M_V considered. Applying this transformation, the probability functions can be expressed as $P(\log(SFR))$ — the transformed probability functions are shown in Fig. 6. Also shown is the observationally estimated range of SFR for the actual $z = 2.58$ DLA (Fynbo et al. 2013). As can be seen, the probability functions all peak in the observational SFR range - this is also an important results of this work. To be more quantitative, the

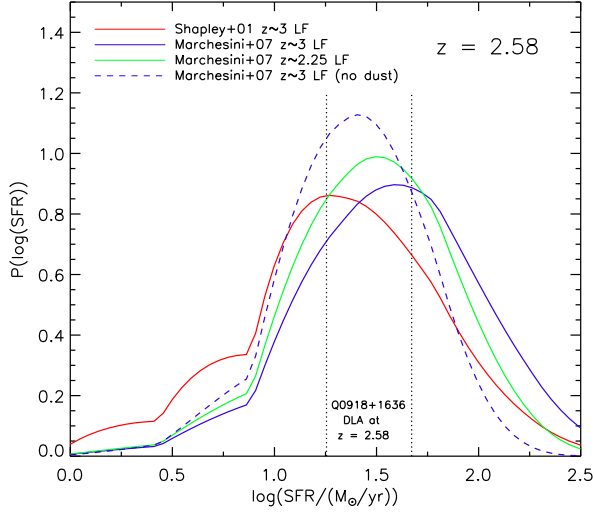


Figure 6. Probability distributions, $P(\log(SFR))$, for the three different extinction corrected LFs (S01: red curve, M07 $z\sim 3$: blue, solid curve, M07 $z\sim 2.25$: green curve). Also shown, is the $P(\log(SFR))$ resulting from not extinction correcting the M07 $z\sim 3$ LF (blue, dashed curve). Finally shown, by vertical dotted lines, is the observationally estimated SFR range for the $z = 2.58$ DLA (Fynbo et al. 2013)

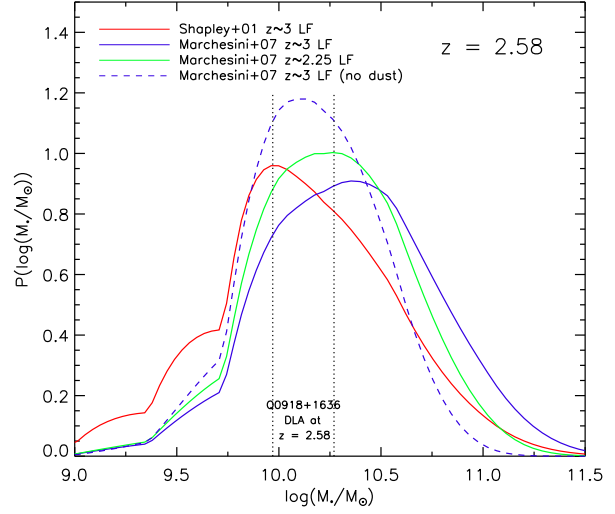


Figure 8. Probability distributions, $P(\log(M_*))$, for the three different extinction corrected LFs (S01: red curve, M07 $z\sim 3$: blue, solid curve, M07 $z\sim 2.25$: green curve). Also shown, is the $P(\log(M_*))$ resulting from not extinction correcting the M07 $z\sim 3$ LF (blue, dashed curve). Finally shown, by vertical dotted lines, is the observationally estimated $1-\sigma$ range for the $z = 2.58$ DLA (Fynbo et al. 2013)

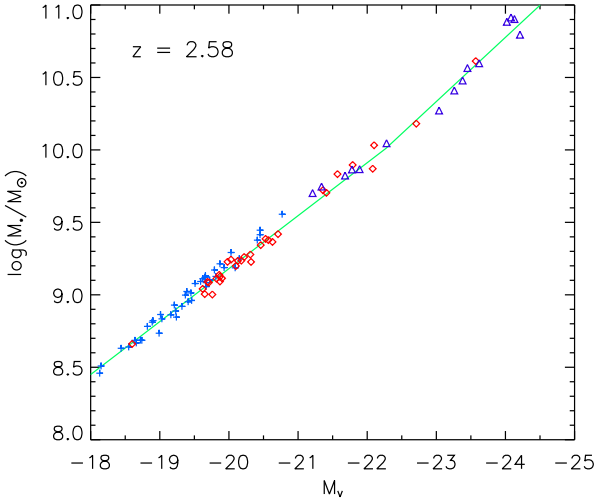


Figure 7. Relation between $\log(M_*)$ and M_V for the simulated galaxies at $z=2.58$. The rescaled HR halo simulations are shown by dark blue triangles (15 galaxies), the unscaled HR simulations by red squares (32 galaxies) and the HR disk galaxy simulations by light blue crosses (48 galaxies). Also shown is a two-component linear fit to the data.

probability of finding an SFR in the range $10-100 M_\odot/yr$ is determined. For the extinction corrected LFs, this probability is 0.65, 0.75 and 0.78. For the non extinction corrected M07 $z\sim 3$ LF, the corresponding probability is 0.79. Hence, a central result of this paper is that, based on the new galaxy formation models, a) extreme galaxies are not required to explain the observed $z = 2.58$ DLA, and b) good agreement with the observed DLA is found.

For additional comparison to observations, it is also convenient to express the probability functions as functions of galaxy

stellar mass. In Fig. 7 the relation between M_* and M_V is shown for the 95 HR sample galaxies. It is seen, that there is a quite tight relation between the two quantities. The relation can be well fitted by a two component linear relation shown in the figure:

$$\log(M_*) = \begin{cases} -0.3643M_V + 1.893, & M_V \geq -22.27, \\ -0.4462M_V + 0.068, & M_V < -22.27, \end{cases} \quad (30)$$

Applying this transformation, the probability functions can be expressed as $P(\log(M_*))$ — the transformed probability functions are shown in Fig. 8. Also shown is the observationally estimated range of M_* for the actual $z = 2.58$ DLA (Fynbo et al. 2013). As can be seen, the probability functions all peak in or near the observational M_* range.

3.4 Kinematics

From the GALFIT analysis Fynbo et al. (2013) infer a (projected) axis ratio of the DLA galaxy of $b/a = 0.43$. The system may be described as disk-like, given the elongated shape, and the fact that the Sérsic n close to 1. Fynbo et al. (2013) argue that the inclination angle of the (potential) disk galaxy is about $i \simeq 60$ deg.

Moreover, the position of the QSO (and hence the DLA absorbing gas) on the sky is located at an angle of about $\phi \sim 45$ deg. relative to the major axis of the DLA galaxy. The velocity centroid of the [OIII] $\lambda 5007$ line is $36 \pm 20 \text{ km s}^{-1}$ blue-shifted compared to the center of the low-ionization absorption lines (Fynbo et al. 2013).

It is clearly of interest to determine whether the simulated galaxies display signatures of disk-like kinematics, in particular in relation to the observed DLA galaxy:

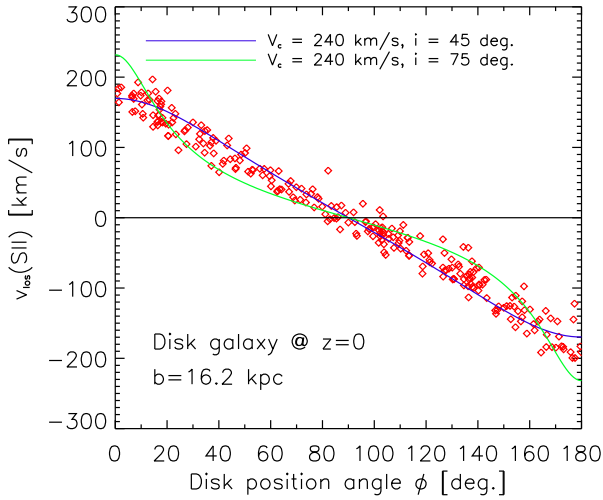


Figure 9. For an ideal, plane disk in circular rotation with constant rotation velocity of 240 km s^{-1} is shown the expected $v_{\text{los}}(\phi)$ (eq. (31)) for inclination angles $i = 45$ and 75 deg. Also shown, for a $z = 0$ disk galaxy with an extended gas disk, are $n(\text{SII})$ weighted line-of-sight velocities for the subset 600 $b=16.2$ kpc sight-lines which have $\log(N(\text{SII})) \geq 15.82$ and are hitting the disk at angles between 15 and 45 deg., corresponding to inclination angles between 45 and 75 deg.

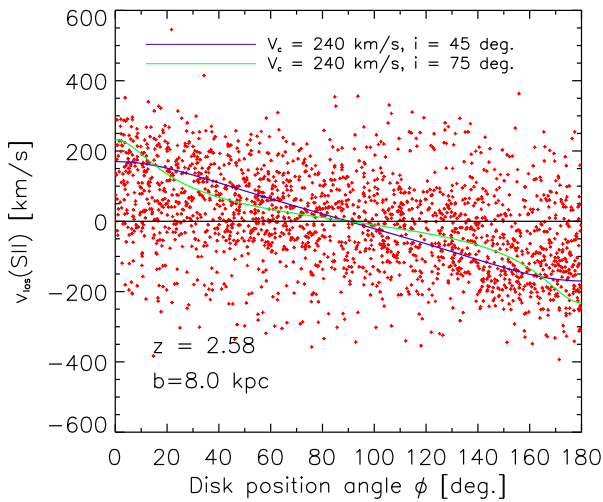


Figure 10. For all $z=2.58$ galaxies, which are characterized by having at least one $b=16.2$ kpc sight-line with $\log(N(\text{SII})) \geq 15.82$, are shown $n(\text{SII})$ weighted line-of-sight velocities for the subset of 600 $b=8.0$ kpc sight-lines which have $\log(N(\text{SII})) \geq 15.82$ and are hitting the galaxy at angles between 15 and 45 deg., corresponding to inclination angles between 45 and 75 deg. The curves shown are the same as in Fig. 9.

3.4.1 Signatures of disk-like kinematics for the simulated galaxies

Consider a planar disk with gas in constant circular rotation of velocity V_0 , and let the inclination angle with the plane of the sky be i (assumed in the following to be larger than zero). Denoting the total angular momentum of the disk by \mathbf{J} , a unit vector along \mathbf{J} will be $\mathbf{j}=\mathbf{J}/|\mathbf{J}|$. Assuming the x-y plane to be the plane of the

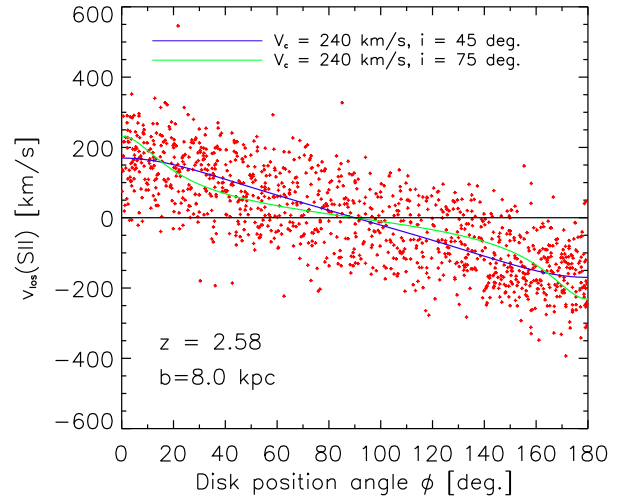


Figure 11. Same as Fig. 10, but restricted to the subset of galaxies displaying a young stellar disk *and* a gaseous disk-like structure, approximately aligned with the stellar disk.

sky, with origo at the center of the disk, and oriented such that the unit vector projected onto the plane of the sky is parallel with the y-axis ($\mathbf{j}_{x,y} = (0, j_y)$), then the largest gas line-of-sight recession velocity will be observed along the positive x-axis, and the largest approaching velocity will be observed along the negative x-axis.

For a given x-y position in the disk’s projection onto the plane of the sky, we shall denote the absolute value of the angle between the positive x-axis and the direction from the center to the position by ϕ (so ϕ is measured either clock-wise or anti-clock-wise from the positive x-axis, depending on the location of the x-y position and takes values between 0 and 180 degrees). It is then straightforward to show that the line-of-sight velocity of gas located at “projected disk position angle” ϕ , is given by

$$v_{\text{los}} = V_0 \frac{\sin(i)}{\sqrt{1 + \left(\frac{\tan(\phi)}{\cos(i)}\right)^2}}, \quad (31)$$

First, we test how well the above expression describes what is found for a $z = 0$ disk galaxy with an extended gaseous disk. The galaxy has an almost constant rotation curve of amplitude $V_0 \simeq 240 \text{ km s}^{-1}$, and is taken from the sample of disk galaxy simulations described in sec. 2.5. As in sec. 3.1, 600 sight-lines are shot through the disk at impact parameter $b = 16.2$ kpc, and the analysis is then performed in exactly the same way as in that section. In Fig. 9 is shown a) results of eq. (31) for inclination angles $i = 45$ and 75 deg., and b) $n(\text{SII})$ weighted line-of-sight velocities for the subset of the 600 sight-lines which have $\log(N(\text{SII})) \geq 15.82$ and are hitting the disk at angles between 15 and 45 deg., corresponding to inclination angles between 45 and 75 deg. As can be seen from the figure, the line-of-sight velocities in general fall close to the predictions by eq. (31). Turbulent velocities appear to be at the level $\sigma \sim 10 - 20 \text{ km s}^{-1}$, consistent with what is found observationally for cold $z = 0$ disks.

Next, we analyze the $z = 2.58$ galaxies for similar kinematic signatures. We first shoot 600 sight-lines at $b = 8$ kpc, to obtain better statistics and a more clear-cut picture of the kinematic state of the galaxies. The result for all sight-lines with $\log(N(\text{SII})) \geq 15.82$ and for all galaxies is shown in Fig. 10. The turbulent velocity dispersion is now much larger (of the order 100 km s^{-1} — see be-

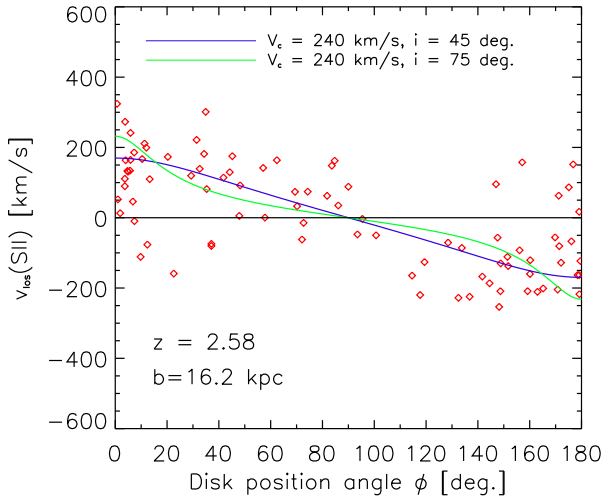


Figure 12. Same as Fig. 11, but now for $b=16.2$ kpc sight-lines.

low), but there is still a clear correlation between $v_{\text{los}}(\text{SII})$ and disk galaxy position angle ϕ (the two quantities are correlated at the $20\text{-}\sigma$ confidence level). This hints the presence of rotational motion in at least some of the $z = 2.58$ galaxies. Third, to elaborate further on this, all $z = 2.58$ galaxies with $\log(N(\text{SII})) \geq 15.82$ sight-lines at $b = 16.2$ kpc were visually inspected. The subset of galaxies displaying a young stellar disk *and* a gaseous disk-like structure, approximately aligned with the stellar disk were selected — the stellar disks typically have an extend of $R \sim 5$ kpc, and the gaseous disks typically extend to $R \sim 10$ kpc. In Fig. 11, we show the relation between $v_{\text{los}}(\text{SII})$ and ϕ for this case, which comprises 56% of all the sightlines shown in Fig. 10. The correlation now stands out very clearly, and is statistically significant at the $41\text{-}\sigma$ confidence level.

Finally, we perform the analysis of the disk-like galaxies for impact parameter $b = 16.2$ kpc. The result of this is shown in Fig. 12. As can be seen, the correlation is still present, but, as one would expect, not so pronounced at these large galactocentric distances. The correlation is statistically significant at the $8\text{-}\sigma$ confidence level, so we conclude that at least a subset of the galaxies display disk-like motion even at galactocentric distances $R \gtrsim 23 - 60$ kpc, depending on the inclination angle. We note, however, that this result has been obtained in a somewhat subjective way, but also that the observed candidate DLA galaxy does display a disk-like morphology and a Sérsic n close to 1.

3.4.2 Kinematical comparison to the DLA galaxy

As mentioned above, the gas traced by the low-ion absorption lines is receding by a line-of-sight velocity of 36 ± 20 km s $^{-1}$ compared to the velocity centroid of the [OIII] $\lambda 5007$ emission line. The emission originates from the central parts of the DLA galaxy, and our working hypothesis is that this line traces the systemic velocity of the DLA galaxy. Moreover, the absorbing gas is located at a disk position angle $\phi \sim 45$ deg. (or 135 deg. depending on the rotational direction of the disk-like structure — see further below).

For comparison to the observed DLA galaxy, we determine the average line-of-sight velocity of the SII absorbing gas along the $\log(N(\text{SII})) \geq 15.82$ sight-lines of the “disk-like” simulated galax-

ies: For sight-lines located such that $30 < \phi < 60$ deg., we find $\bar{v}_{\text{los}} = 102 \pm 21$ km s $^{-1}$, and a velocity dispersion of $\sigma = 109$ km s $^{-1}$. Considering sight-lines located such that $120 < \phi < 150$ deg., one obtains $\bar{v}_{\text{los}} = -137 \pm 23$ km s $^{-1}$, and a velocity dispersion of $\sigma = 103$ km s $^{-1}$. Combining the two ϕ -angle intervals, exploiting the symmetry expected in the case of a rotating disk (i.e., changing the sign of the $120 < \phi < 150$ deg. velocities), results in $\bar{v}_{\text{los}} = 118 \pm 15$ km s $^{-1}$ and a velocity dispersion of $\sigma = 106$ km s $^{-1}$ for $30 < \phi < 60$ deg. (and $\bar{v}_{\text{los}} = -118 \pm 15$ km and a velocity dispersion of 106 km s $^{-1}$ for $120 < \phi < 150$ deg.). All results refer to inclination angles i between 45 and 75 deg., as above.

If the “disk” of the DLA galaxy, as a whole, is indeed “rotating” away from us in the region probed by the DLA absorption with average line-of-sight velocity of 118 km s $^{-1}$, then the deviation between this and the measured line-of-sight velocity of 36 km s $^{-1}$ amounts to 82 km s $^{-1}$. With a velocity dispersion of $\sigma = 106$ km s $^{-1}$, this amounts to about 0.8σ , so the measured value of 36 km s $^{-1}$ is quite consistent with the models. If, on the other hand, the DLA galaxy is “rotating” towards us with an average line-of-sight velocity of -118 km s $^{-1}$, then the deviation between this and the measured $+36$ km s $^{-1}$ amounts to 154 km s $^{-1}$ or about 1.5σ . Hence, it is about a factor of three more likely that the “disk” as a whole is receding rather than advancing in the region probed by the DLA absorption.

For the idealized disk described above, and for $V_0 = 240$ km s $^{-1}$ and $\phi = 45$ deg., it follows from eq. (31) that $v_{\text{los}} = 98$ km s $^{-1}$ for $i = 45$ deg. and 58 km s $^{-1}$ for $i = 75$ deg. The average value of 118 ± 15 km s $^{-1}$ and dispersion of 106 km s $^{-1}$ obtained above hence indicates that the circular velocities of the disk-like galaxies are somewhat larger than 240 km s $^{-1}$ at radii $\sim 15 - 30$ kpc from the centers of the galaxies. Indeed, the circular velocities of these galaxies are found to lie in the range $290\text{-}360$ km s $^{-1}$.

4 DISCUSSION

4.1 UVB self-shielding and radiative effects of local young stars

Adopting the mean field approximation of Rahmati et al. (2013), it is assumed in the analysis and in the simulations, that the local radiation field, at a given redshift, depends mainly on the local hydrogen number density $n_H(\mathbf{x})$. According to Rahmati et al. (2013) this is an excellent approximation, but it is still of value to test other scenarios: The first alternative considered, is the assumption that effects of neutral gas shielding can be completely neglected, i.e., assuming that the gas everywhere is exposed to the full UVB. This obviously is an extreme case, as medium to high density gas will provide some shielding of the UVB.

4.1.1 Neglecting self-shielding of the UVB

To test this case, all HR simulations were run for a period of 100 Myr till $z = 2.58$, with UVB self-shielding switched off, i.e. the gas is assumed to be exposed to the full UVB, independent of gas density. To make the simulations self-consistent, the radiative cooling and heating functions were appropriately modified using Cloudy. So the new simulations were started from the original simulations at $z = 2.67$ and run for the 100 Myr period to $z = 2.58$ with the modified simulation code. The 100 Myr period allows plenty of time for the new ionization balances to be established.

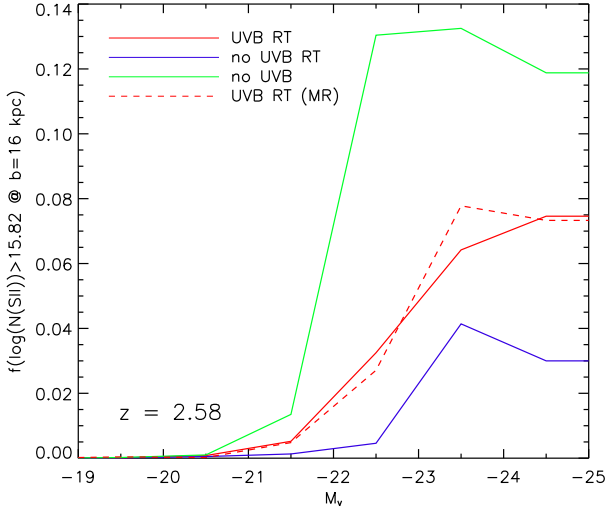


Figure 13. For various assumptions about the UVB self-shielding, is shown the probability of finding $\log(N(\text{SII})) \geq 15.82$ for a sight-line at impact parameter $b = 16.2$ kpc relative to a given galaxy of absolute magnitude M_V at $z=2.58$. The red solid curve corresponds to the mean field approximation UVB self-shielding employed in this paper (already shown in Fig. 3 on a log scale), the blue curve corresponds to the case of no UVB self-shielding, i.e., the gas is everywhere exposed to the full, unimpeded UVB, and the green curve corresponds to the case of no H-ionizing UVB at all, i.e., it is assumed that the $E \geq 13.61$ eV part of the UVB has been completely blocked by neutral hydrogen absorption. The red dashed curve corresponds to the fiducial case, but is based on medium resolution simulations. For more detail, see the text.

Since all gas in this case is exposed to the full, unimpeded UVB, higher ionization stages will be more populated for most atoms, including Sulfur, compared to the fiducial model. As can be seen from Fig. 13, the fraction of $b=16.2$ kpc sight-lines of $\log(N(\text{SII})) \geq 15.82$ per galaxy is indeed lower than for the fiducial model. In particular, around $M_V \sim -22$ the decrease is very significant. This implies that the peak of the conditional probability function is shifted somewhat towards larger luminosities. This is shown in Fig. 14, where $P(\log(\text{SFR}))$ is shown for the M07 $z \sim 2.25$ LF in the no self-shielding case, together with the fiducial case.

4.1.2 Neglecting the H-ionizing part of UVB

As another extreme case, we now consider the case where it is assumed that all UVB H-ionizing photons have been absorbed, such that the gas is fully shielded from H-ionizing photons. UVB photons of energy less than 13.61 eV are still assumed to be transmitted — this is important for the population of SII, since the ionization potential for singly ionizing neutral Sulfur is 10.36 eV.

To test this case, all HR simulations were run for a period of 100 Myr till $z = 2.58$, with H-ionizing UVB switched off, i.e. the gas is assumed to be fully shielded. To make the simulations self-consistent, the radiative cooling and heating functions were appropriately modified using Cloudy. So, as for the no UVB RT case, the new simulations were started from the original simulations at $z = 2.67$ and run for the 100 Myr period to $z = 2.58$ with the modified simulation code. Since all gas in this case is shielded, higher ionization stages will be less populated for most atoms, including Sulfur, compared to the fiducial model. As can be seen from Fig. 13, the fraction of $b=16.2$ kpc sight-lines of

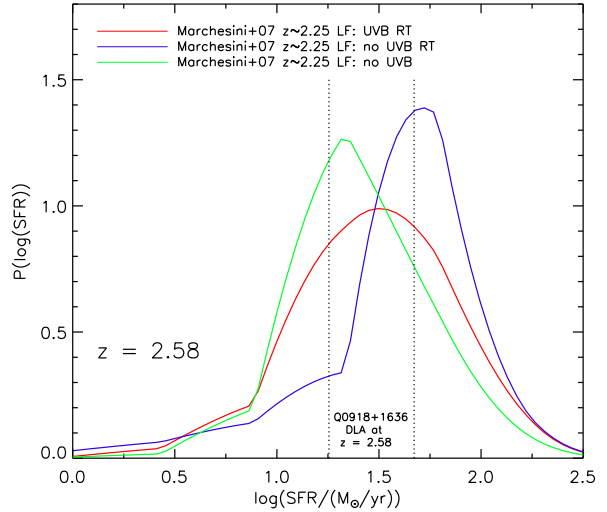


Figure 14. Dependence of the probability distributions $P(\log(\text{SFR}))$ on the details of the UVB self-shielding. The extinction corrected M07 $z \sim 2.25$ LF is used as an example, and the curves are labeled as in Fig. 13.

$\log(N(\text{SII})) \geq 15.82$ per galaxy is higher than for the fiducial model. In particular, around $M_V \sim -22$ the increase is quite significant. This implies that the peak of the conditional probability function is shifted somewhat towards lower luminosities. This is also shown in Fig. 14 (again for the M07 $z \sim 2.25$ LF). Focusing on the probability of finding an SFR in the range $10\text{--}100 M_\odot/\text{yr}$, we find for the M07 $z \sim 2.25$ LF that this probability is 0.82 for the no UVB self-shielding case and 0.80 for the no UVB case, so in both cases marginally larger than the 0.78 for the fiducial case.

4.1.3 Radiative effects of young stars in the galaxy

Only radiative effects of the UVB are considered in the fiducial model. Even though an impact parameter of 16.2 kpc at $z = 2.58$ implies that the galaxy is being probed in its outer parts, radiation from the young stars in the galaxy may in principle still affect the ionization balances in the gas in the outer parts of the galaxy, in particular radiation of $E < 13.61$ eV — see below.

Focusing first on H-ionizing radiation, we calculate for each line-of-sight the minimum distance to any star particle of age less than 10 Myr in the galaxy. For galaxies where $b=16.2$ kpc sight-lines of $\log(N(\text{SII})) \geq 15.82$ are present, the average over these minimum distances are then calculated for each galaxy. Finally, the average over all such galaxies is calculated. The result obtained is $\langle d_{\text{min},10\text{Myr}} \rangle = 3.7 \pm 0.3$ kpc. The galaxies for which high metallicity $b=16.2$ kpc sight-lines are found typically to have disk-like morphology, with the bulk of the SII absorption arising in or near the “disk”. For densities $n_H \sim 1 \text{ cm}^{-3}$, typical HII region radii are an order of magnitude smaller than $\langle d_{\text{min},10\text{Myr}} \rangle$ (e.g., McCray & Kafatos (1987)), so it is unlikely that H-ionizing radiation from young stars in the galaxy affects the ionization balance along the sight-lines probed. In addition, in section 5 it will be argued that the α -elements, like Sulfur, found in the outer galaxy mainly were produced by evolving stars in the inner galaxy, and subsequent transported outward by galactic winds. Hence, young, UV emitting stars are expected to be located in the inner galaxy ($r \lesssim 10$ kpc — see section 5), whereas the metal-rich gas probed

by the $b=16.2$ kpc sight-lines will be located at galactocentric distances of $r \gtrsim 15 - 30$ kpc.

For radiation of $E < 13.61$ eV the situation is quite different, however. Such radiation is transmitted almost unimpeded through the interstellar gas (apart from at or near the Lyman line wavelengths). Since the ionization potential of neutral Sulfur is 10.36 eV, we shall, for the purposes of the present work, focus on the radiation energy interval 10.36-13.61 eV. For each sight-line, we calculate at each “grid-point” the total flux at $\lambda = 1105 \text{ \AA}$ from all stars in the galaxy of age less than 34 Myr (the lifetime of a $9 M_{\odot}$ star), using the Starburst99 models (Leitherer et al. 1999). We then calculate, for each sight-line, the n_{SII} weighted $\lambda = 1105 \text{ \AA}$ flux. For all $b=16.2$ kpc sight-lines of $\log(N(SII)) \geq 15.82$, we subsequently calculate the average $\lambda = 1105 \text{ \AA}$ flux for the galaxy, and finally we average over all such galaxies. It is found, that the flux from the young stars is about twice the flux of the UVB at 1105 \AA , so in principle this contribution could be important for the ionization balance. To investigate this further, we produced artificial UVBs, where the flux in the energy interval 10.36-13.61 eV was increased by a factor of 100 relative to the Haardt & Madau (2012) UVBs. We then proceed as before, using Cloudy to determine SII densities etc. It is found, that the results of this are almost indistinguishable from the fiducial case. We conclude that the effects of radiation from young stars in the galaxies are unimportant for the purposes of this work.

4.2 Non-local SII absorption

The galaxies considered in this work have all been simulated using the “zoom-in” technique (sec. 2.5). The advantage of the technique is that high resolution is achieved in and near the galaxy — the disadvantage, however, is that the galaxy region is only well resolved out to ~ 100 -200 kpc from the center of the galaxy. This can potentially be problematic, since a non-local galaxy, of lower luminosity and with the QSO located at smaller impact parameter than the $b=16.2$ kpc “candidate galaxy”, could in principle be responsible for the DLA absorption. Assuming that the redshift of the “candidate galaxy” is known, e.g., from [OIII] $\lambda 5007$ or H α emission, obviously secondary, non-local galaxies situated sufficiently far along the line-of-sight can be identified as not associated with the “candidate galaxy” from the velocity difference. But for velocity differences of ~ 500 km/s or less, the case is less clear cut. Assuming pure Hubble flow at $z = 2.58$, this would correspond to distances of ~ 2 physical Mpc, or ~ 7 co-moving Mpc. To address the effects of non-local galaxies quantitatively, a small-scale cosmological hydro/gravity simulation, previously run to $z = 2.51$ and based on a Salpeter (1955) IMF and a previous SN feedback scheme (e.g., Sommer-Larsen (2006)) is utilized. The simulation volume is part of the dark matter only cosmological volume described in sec. 2.5. The (cubical) small-scale cosmological simulation has a box-length of $l=3.2$ physical Mpc or 11.5 co-moving Mpc. As this box-length is somewhat small for the present purpose, the box is replicated to create a larger cubical box, of box-length $L=9.6$ physical Mpc or 34.4 co-moving Mpc and consisting of $3^3 = 27$ of the original boxes.

To determine the probability of detecting $\log(N(SII)) \geq 15.82$ as a function of impact parameter, for each of the presently simulated galaxies, 200 sight-lines are shot randomly through each galaxy at impact parameters $b = 1, 2, 3, \dots, 25$ kpc. The galaxies are then binned according to stellar mass, and a probability function $P_{15.82}(b, M_{\star})$ is constructed. The probability function thus obtained is shown in Fig. 15 for 7 different stellar galaxy masses. For

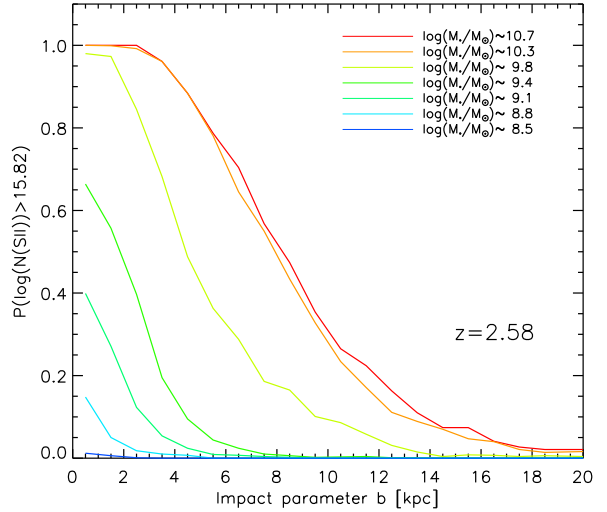


Figure 15. Probability function $P_{15.82}(b, M_{\star})$ shown for 7 different values of stellar galaxy mass, M_{\star} .

each of the 589 galaxies located in the central $l=3.2$ physical Mpc box, 1000 lines-of-sight are shot through the full, replicated box, each at an impact parameter of $b=16.2$ kpc relative to the galaxy. The directions of the 1000 lines-of-sight are chosen at random, and lines-of-sight which intercept a brighter non-local (see below) galaxy at impact parameter $b \leq 16.2$ kpc are rejected (see 3.1). In this way, for each of the 589 galaxies and for each line-of-sight, the quantity

$$\tau_{15.82} = \sum_{i=1}^n P_{15.82}(b_i, M_{\star,i}) , \quad (32)$$

is determined, where the sum is taken over all galaxies in the large box, situated at distances of 200 kpc or more from the galaxy under consideration and intercepted at $b \leq 25$ kpc. In practice, it turns out that for any of the sight-lines probed, at most one such non-local galaxy in the replicated box contributes with $N(SII) \geq 10^{15.82} \text{ cm}^{-2}$.

Subsequently, for each of the 589 galaxies the average of $\tau_{15.82}$ over the 1000 lines-of-sight, $\langle \tau_{15.82} \rangle$, is calculated, and finally, by binning the 589 galaxies according to M_V , the probabilities of non-local SII absorption, $p_{15.82, \text{non-local}}(M_V)$ are determined. To obtain a larger dynamical range, the calculations are repeated with the replicated box scaled by a (linear) factor of 1.6, and galaxy masses scaled by a factor of 1.6^3 . The resulting non-local SII absorption probability functions are displayed in Fig. 3. As can be seen from the figure, for the relevant values of M_V , the probability of non-local SII absorption is 2-3 orders of magnitude less than the probability of absorption in or near the galaxy itself. To first order, it is hence justified to exclude effects of non-local absorption from the analysis. The average path-lengths for the unscaled and scaled replicated boxes are 40 and 66 cMpc, respectively. Assuming pure Hubble flow, this corresponds to velocity shifts of about 3000 and 4800 km/s, respectively, which should be easily detectable. Hence, the box-sizes used for the non-local effects analysis seem sufficiently large.

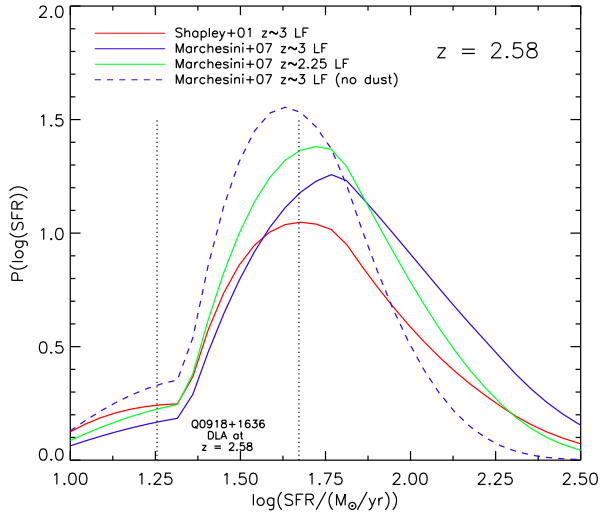


Figure 16. Constrained probability distributions of galaxy SFR for the case $\log(N(\text{SII})) \geq 16.20$ and $b=16.2$ kpc — symbols as in Fig. 6

4.3 Effects of possible Sulfur depletion into dust grains

In this subsection, effects of (hypothetical) depletion of Sulfur into dust grains is discussed: Sulfur is only weakly depleted into dust grains (e.g., Fitzpatrick & Spitzer (1997), but recent work indicates that some amount of depletion may take place — see, e.g., Calura et al. (2009) and Jenkins (2009).

Fynbo et al. (2011) obtain $\log(N(\text{SII})) = 15.82 \pm 0.01$, and $\log(N(\text{ZnII})) = 13.40 \pm 0.01$ for the DLA. This corresponds to “metallicities” of $[\text{SII}/\text{H}] = -0.26 \pm 0.05$ and $[\text{ZnII}/\text{H}] = -0.12 \pm 0.05$, respectively. As Zinc can be assumed to be un-depleted by dust, this could be taken to indicate a small amount of Sulfur depletion, although, given the uncertainties, the effect is small. As Sulfur is an α -element, we moreover (conservatively) assume that $[\alpha/\text{Fe}] = 0.24$ at $z=2.58$ (based on the simulations). Assuming that Zn traces iron, this all in all implies that $\log(N(\text{SII})) = 16.20$ should be a conservative upper limit to the SII column density of the DLA.

The analysis described in sections 3.1 and 3.3 is then re-performed, but now for $\log(N(\text{SII})) \geq 16.20$, rather than 15.82. The resulting constrained probability distributions of galaxy SFR are shown in Fig. 16. As can be seen from the figure, the peaks of the probability functions move towards larger SFR, but they are still located close to the observed SFR of the proposed DLA galaxy counterpart. Moreover, the probability of finding an SFR in the range $10\text{--}100 M_{\odot}/\text{yr}$ is 0.85, 0.79 and 0.88 for the three extinction corrected LFs considered. For the non extinction corrected M07 $z \sim 3$ LF, the corresponding probability is 0.94. Hence, the main results obtained in section 3.3 still hold, if the “true” SII column density is $10^{16.20} \text{ cm}^{-2}$.

4.4 Statistical effects

Given that the probabilities $f_{15.82}(M_V)$ shown in Fig. 3 are based on 95 sample galaxies, the constrained probability functions derived in 3.3 will be affected by statistical effects. In order to assess the importance of these effects we carried out 1000 Monte-Carlo simulations. Each of the seven $f_{15.82}(M_V)$ were assumed to be normally distributed with mean values and dispersions set to the values inferred from the 95 sample galaxies, as shown in Fig. 3.

For each MC realization of the $f_{15.82}(M_V)$'s, the constrained probability functions were constructed, and on the basis of these, the average SFRs corresponding to this realization were determined for each of the luminosity function models. Based on the 1000 MC realizations, the average SFRs determined were 36, 56, 43 and 32 M_{\odot}/yr , with dispersions of 4, 6, 4 and 3 M_{\odot}/yr , for the S01, M07 $z \sim 3$, M07 $z \sim 2.25$ and M07 $z \sim 3$ (no dust-correction) LFs, respectively. For the actual set of $f_{15.82}(M_V)$'s (Fig. 3) and corresponding probability functions (Fig. 6), we find average SFRs of 36, 57, 42 and 32 M_{\odot}/yr for the four LFs, respectively. Hence, there is no indication that statistical effects affect the main conclusions obtained in this paper.

4.5 Numerical resolution

It is important to check that the results obtained do not depend on the resolution of the numerical simulations. To address this, we go through the analysis described in section 3, using the MR simulations rather than the HR simulations. The MR simulations have four times lower mass resolution than the HR simulations. As can be seen from Fig. 13, the fraction of $b=16.2$ kpc sight-lines of $\log(N(\text{SII})) \geq 15.82$ per galaxy as a function of M_V is quite similar to what is found for the fiducial model. To quantify this, probability functions are determined on the basis of the MR simulations, as described in section 3. These are used to calculate average SFRs for the four cases considered in the previous subsection. One obtains 38, 59, 45 and 34 M_{\odot}/yr , quite close to what is found for the HR simulations.

4.6 Lack of AGN feedback

The present simulations do not include effects of feedback from supermassive black holes (BHs) — below we comment briefly on this possible shortcoming.

The formation and evolution of BHs is thought to be linked to galaxy evolution. Correlations between black hole mass and galaxy properties indicate a considerable degree of co-evolution (e.g. Richstone et al. 1998; Ferrarese & Merritt 2000; Gebhardt et al. 2000; Marconi & Hunt 2003; Häring & Rix 2004). The energy released by Active Galactic Nuclei (AGNs) is likely liberated in connection with accretion of matter onto the BH. AGN hence provide a physical link between black hole growth and the broader galaxy (e.g. Silk & Rees 1998; Di Matteo et al. 2005). Yet the physical processes of black hole fueling that trigger AGN are not fully understood.

Simulations show that major mergers funnel gas toward the central black holes (Hernquist 1989; Barnes & Hernquist 1992; Di Matteo et al. 2005), but although mergers probably do enhance BH activity (Ellison et al. 2011), observations have not strongly supported the major merger scenario for most AGNs: AGNs are typically located in isolated galaxies, with no obvious signs of a major merger (Grogin et al. 2005; Pierce et al. 2007; Gabor et al. 2009; Georgakakis et al. 2009).

As AGNs are common in star-forming disks (Hwang et al. 2010; Cisternas et al. 2011; Kocevski et al. 2012; Schawinski et al. 2012; Juneau et al. 2013), it is of interest to study the interplay between the star-forming gas in (gas-rich) disk galaxies and a central BH using very high numerical resolution in order to resolve as well as possible the processes occurring in the central galaxy. Gabor & Bournaud (2013) performed such a study using AMR (adaptive mesh refinement) at a resolution of 6 pc. They focused on the thermal feedback from the AGN, and although the

AGN drives uni/bi-polar outflows vertical to the disk at the center of the galaxy (expansion along the path of least resistance, cf. Faucher-Giguère & Quataert (2012)) the star-formation in the disk in general is only very weakly affected. Roos et al. (2015) followed up on this work, and showed that taking in addition also the radiation feedback from the AGN into account (even at quasar luminosities) still only affects the general star-formation in the disk very little. To be conservative, the authors even neglected the partial absorption of UV and X-ray photons by the (putative) dusty torus. Newton & Kay (2013) reached similar conclusions to the above based on their simulations of AGN feedback in isolated galaxies.

Taken at face value, these results could hint that the omission of AGN feedback in the current work is not a major limitation. However, as pointed out by the authors, they study isolated galaxies, and AGN feedback might still affect galaxy evolution in a cosmological context. Also, the apparent “quenching” of late time star formation observed for some (typically massive) galaxies (“red and dead” galaxies) may be interpreted most simply as an effect of AGN feedback (e.g. Bower et al. 2006; Croton et al. 2006).

We plan to include effects of AGN feedback in future work.

5 HOW WAS THE HIGH METALLICITY GAS IN THE OUTER GALAXY ENRICHED?

As has been argued in this work, the SII absorbing gas is most likely associated with the DLA galaxy. It is hence of considerable interest to investigate how this metal rich gas, located at galactocentric distances of $\sim 15 - 30$ kpc, was enriched. Possible mechanisms include a) the gas is located in a disk like structure, already in place at $z=2.58$, and has been enriched locally through *in situ* star formation, b) the metal rich gas has been stripped off passing satellite galaxies, and c) the enriched gas has been deposited in the outskirts of the galaxy through the effects of metal enriched winds ejecting gas and metals from the inner parts of the DLA galaxy. In the following it will be argued that mechanism “c” is by far the most important.

Due to the Lagrangian nature of SPH, it is possible to trace a given fluid element (SPH particle) back in time. Hence, the position history, thermal history, enrichment history etc. can be determined for the fluid element. The time resolution will be set by how often the simulation state is saved — in the present case, once per 100 Myr. In the following, this capability of determining the history of each SPH particle will be used to determine the position of SPH particles of interest during their major metal enrichment episodes.

To facilitate the analysis, it will be restricted to SPH particles that are rich in SII at $z=2.58$. Specifically, only SPH particles with an abundance of *singly ionized* Sulfur exceeding the (total) solar Sulfur abundance, i.e.

$$Z_S \cdot f_{\text{SII}} > Z_{S,\odot}, \quad (33)$$

are considered in the analysis. It may seem overly restrictive to consider only such very SII-rich particles, but it turns out that for $\log(N(\text{SII})) \geq 15.82$ sight-lines at $b = 16.2$, $\sim 75\%$ of the contribution to $N(\text{SII})$ (eq. (22)) stems from such particles. Moreover, for illustrative purposes, the analysis is carried out for just one $z=2.58$ galaxy, of $p_{15.82} \sim 0.05$ and $M_V = -24.02$, but the results for other galaxies are similar.

For the galaxy at $z=2.58$, the Sulfur enrichment histories for all SPH particles located at galactocentric distances between 15 and 30 kpc, and satisfying the above SII-abundance constraint, are determined. Moreover, the positions of the particles relative to the

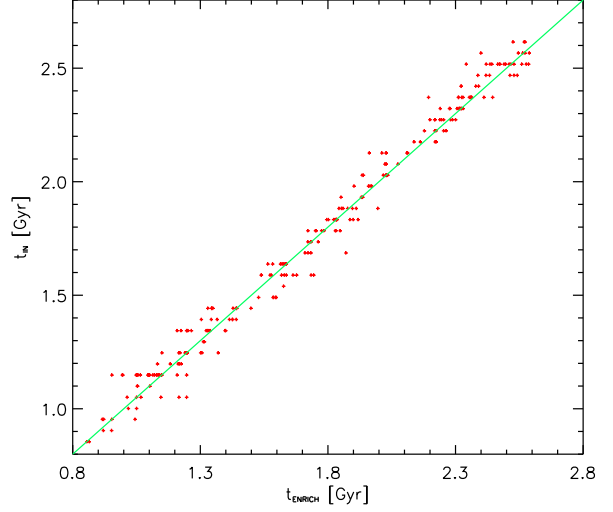


Figure 17. Relation between “inner galaxy time”, t_{in} , and “Sulfur enrichment time”, t_{enrich} , shown by red symbols. Also shown, by the green line, is the relation $t_{\text{in}} = t_{\text{enrich}}$. For more detail, see the text.

proto-galaxy are determined in all relevant time-frames prior to the $z=2.58$ frame (it turns out that, over the time span of interest, the last major merger takes place at $t \sim 0.7$ Gyr, so the main proto-galaxy is well defined at later times).

For each such SPH particle, two characteristic times are determined: 1) The Sulfur enrichment time, t_{enrich} , measures the average time of enrichment of the particle, and is defined as

$$t_{\text{enrich}} = \sum_i \Delta Z_S(t_i) t_i, \quad (34)$$

where $\Delta Z_S(t_i) = Z_S(t_{i+1}) - Z_S(t_i)$, t_i is the time since Big Bang of frame i , and the sum in most cases runs over 20 time-frames dumped at $t = 0.7$ Gyr, 0.8 Gyr, ..., 2.6 Gyr, but see below. 2) The inner galaxy time, t_{in} , measures the average time at which the particle is located in the inner galaxy, and is defined as

$$t_{\text{in}} = \frac{1}{N} \sum_{j=j_{\text{min}}}^{j_{\text{max}}} t_j, \quad (35)$$

where the sum runs over the number of consecutive frames, $N = j_{\text{max}} - j_{\text{min}} + 1$, for which the galactocentric distance of the SPH particle satisfies $r < r_{\text{in}}$. The “inner galaxy radius” is set to $r_{\text{in}} = 10$ kpc, but the main results are not sensitive to moderate variation of this parameter. It turns out that 97% of the SII-rich SPH particles, selected as described above, have been in the inner galaxy from one and up to four times prior to the $z=2.58$ frame. Due to the limited time-resolution of 100 Myr, it is even possible that some fraction of the remaining 3% of SPH particles have also been in the inner galaxy at some point.

Fig. 17 shows the relationship between t_{in} and t_{enrich} . As can be seen from the figure, the two quantities are strongly correlated. Some of the SPH particles have been located in the inner galaxy two or even three times — for these particles, the summation in eq. (34) is performed over the appropriate range of time frames, and two or three data points are shown in Fig. 17 for such particles.

To illustrate the correlation further, in Fig. 18 is shown the distribution of $t_{\text{in}} - t_{\text{enrich}}$ as a histogram. As can be seen from the figure, the width of the distribution is comparable to the time

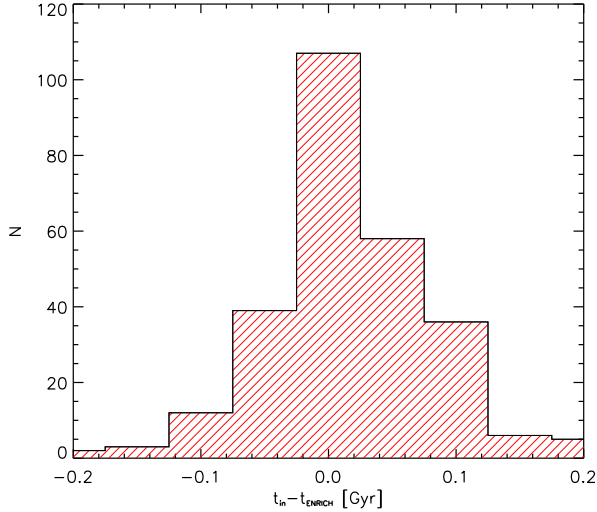


Figure 18. The distribution of $t_{\text{in}} - t_{\text{enrich}}$.

resolution (100 Myr), indicating that the correlation between t_{in} and t_{enrich} is indeed very tight.

The above correlation strongly suggests that the bulk of metal rich SPH particles located in the outer galaxy ($15 < r < 30$ kpc) at $z=2.58$ have been enriched in the inner galaxy. Subsequently, the particles have been deposited in the outer galaxy, likely due to the effects of galactic winds: α -elements like Sulfur are predominantly produced in core collapse (type II) supernovae, and as the SNI explode, metals as well as large amounts of thermal and kinetic energy are injected into the ISM, potentially driving galactic outflows.

To further substantiate the galactic wind scenario, shown in Fig. 19 is the average galactocentric distance, $\langle r \rangle$, of the selected metal rich SPH particles for t_{in} in five bins: $t_{\text{in}} = 1.1-1.3$ Gyr, 1.3-1.5 Gyr etc. As can be seen from the figure, the gas is initially accreted onto the inner proto-galaxy, then expelled to larger radii and eventually re-accreted to $15 < r < 30$ kpc at $z=2.58$. This part of the analysis has been restricted to the subset of particles, which have only been once in the inner galaxy (comprising 71 % of the SPH particles under consideration, i.e., the bulk of the SPH particles), but a similar behavior is found for the SPH particles that are in the inner galaxy on multiple occasions.

In Fig. 20 is shown the median temperature of the SPH particles in the above bins. As can be seen, the gas is initially accreted at a fairly low temperature, $\log(T) \sim 4.2$, and then, at $t \simeq t_{\text{in}}$, heated to $\log(T) \lesssim 6$. Subsequently, as the gas expands (Fig. 19), it cools and the density drops to $n_H \sim 10^{-4} - 10^{-3} \text{ cm}^{-3}$. Eventually, the gas starts re-contracting (this phase is marked by dashed lines in Fig. 20). Despite effects of compressional heating, the temperature continues decreasing (from $\log(T) \simeq 4.5$ to $\log(T) \simeq 4.0$). This is due to the radiative cooling rate being larger than the compressional heating rate, and the temperature balance being set rather by the UVB heating rate. As the density keeps increasing during the re-accretion process, the effect of UVB heating keeps decreasing, and the gas temperature consequently drops.

The focus here has been on Sulfur, which is an α -element, primarily produced by SNIIs. Iron peak elements are also produced abundantly by SNIa's, on a considerably larger stellar evolutionary timescale of the order 1 Gyr (e.g., Lia, Portinari & Carraro 2002a). However, the timescale is sufficiently short compared to the age of

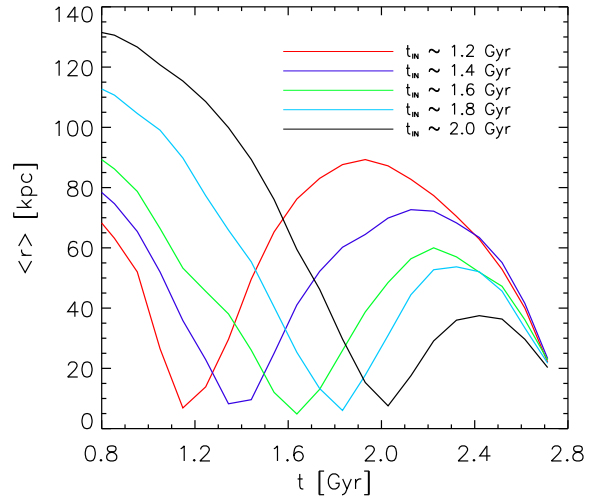


Figure 19. Average galactocentric distance, $\langle r \rangle$, of the selected metal rich SPH particles binned according to the value of t_{in} — for clarity the analysis has been restricted to SPH particles that are only once in the inner galaxy during the time interval under consideration.

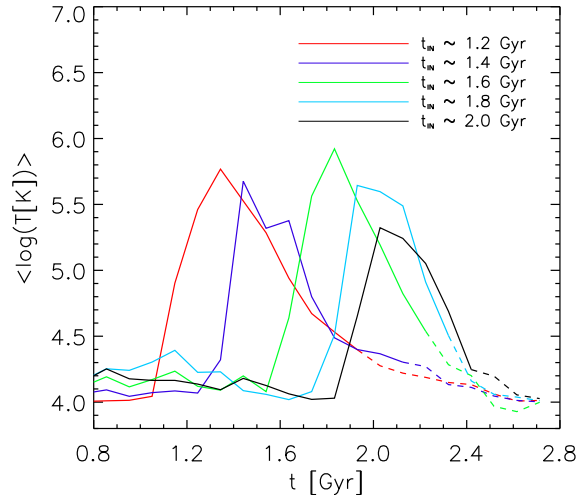


Figure 20. Median temperature of SPH particles in the same t_{in} bins as in Fig. 19. Dashed lines indicate that the SPH particles are in the second accretion phase — see text for details.

the Universe at $z=2.58$, that the outer galaxy may have been enriched by iron from stars exploding as SNIa *in situ* in the outer galaxy. Performing the same analysis as described above (for Sulfur) and restricting the analysis to SPH particles of $[\text{Fe}/\text{H}] > -0.25$ (this results in approximately the same number of SPH particles for the analysis) it is found that 90% of the particles have been located in the inner galaxy one or more times. This indicates that the bulk of the metal rich gas in the outer galaxy was enriched in the inner galaxy and transported outward by winds, but that some additional SNIa enrichment may have taken place *in situ*. Also, if t_{enrich} is based on iron rather than Sulfur, then the relation between t_{in} and t_{enrich} is not as tight as the one displayed in Fig. 17. This again indicates that some *in situ* enrichment by SNIa's may have occurred.

6 CONCLUSION

It is found that a) for $L \sim L_*$ galaxies (at $z=2.58$), about 10% of the sight-lines through the galaxies at impact parameter $b=16.2$ kpc will display a Sulfur II column density of $N(\text{SII}) \geq 10^{15.82} \text{ cm}^{-2}$ (the observed value for the DLA), and b) considering only cases where a near-solar metallicity will be detected at 16.2 kpc impact parameter, the (Bayesian) probability distribution of galaxy star formation rate (SFR) peaks near the value actually observed for the DLA galaxy counterpart of $27^{+20}_-9 M_\odot/\text{yr}$. The probability that the SFR lies in the range 10-100 M_\odot/yr is found to be 0.65-0.80 for a very broad range of assumptions about the $z=2.58$ galaxy luminosity function.

Hence, the main result is that extreme galaxies are not required to match the high impact parameter and high metallicity DLA. In fact, very good agreement between the theoretical predictions and the observed properties of the proposed DLA galaxy counterpart is found. It is shown that this result is very robust, as it is insensitive to large variations in the treatment of UVB self-shielding, statistical uncertainties and possible effects of dust depletion. It is also shown that effects of non-local absorption are unimportant, and the result is shown to hold for a wide range assumptions about the $z=2.58$ V-band luminosity function. Finally, the result is found to be robust to a change of a factor of 4 in the (numerical) mass resolution of the simulations.

It is argued, that the bulk of the α -elements, like Sulfur, traced by the high metal column density, $b=16.2$ kpc absorption lines, have been produced by evolving stars in the inner galaxy, and subsequent transported outward by galactic winds.

ACKNOWLEDGEMENTS

We are grateful to the referee, Simeon Bird, for a number of suggestions and comments, that improved the presentation of this work.

The research leading to these results has received funding from the European Research Council under the European Union's Seventh Framework Program (FP7/2007-2013)/ERC Grant agreement no. EGGS-278202.

The simulations were performed on the facilities provided by HPC/UCPC at University of Copenhagen.

REFERENCES

- Barnes J. E., Hernquist L., 1992, ARA&A, 30, 705
 Behroozi P. S., Conroy C., Wechsler R. H., 2010, ApJ, 717, 379
 Benson A. J., Bower R. G., Frenk C. S., Lacey C. G., Baugh C. M., Cole S., 2003, ApJ, 599, 38
 Bower R.G., Benson A.J., Malbon R., Frenk C.S., Baugh C.M., Cole S., Lacey C.G. 2006, MNRAS 370, 645
 Bower R. G., Benson A. J., Crain R. A., 2012, MNRAS, 422, 2816
 Bower R. G., Benson A. J., Malbon R., Helly J. C., Frenk C. S., Baugh C. M., Cole S., Lacey C. G., 2006, MNRAS, 370, 645
 Bower R. G., McCarthy I. G., Benson A. J., 2008, MNRAS, 390, 1399
 Brook C. B., Kawata D., Gibson B. K., Freeman K. C., 2004, ApJ, 612, 894
 Brook C. B., Stinson G., Gibson B. K., Roškar R., Wadsley J., Quinn T., 2012a, MNRAS, 419, 771
 Brook C. B., Stinson G., Gibson B. K., Wadsley J., Quinn T., 2012b, MNRAS, 424, 1275
 Calura, F., Dessauges-Zavadski, M., Prochaska, J. X., & Matteucci, F., 2009, ApJ, 693, 1236
 Calzetti, D., Armus, L., M., Bohlin, R. C., Kinney, A. L., Koornneef, J. & Storchi-Bergmann, T., 2000, ApJ, 533, 682
 Castor, J., McCray, R., Weaver, R., 1975, ApJ, 200, 107
 Chabrier, G., 2003, Publications of the Astronomical Society of the Pacific, 115, 763
 Cioffi, D.F., McKee, C.F., & Bertschinger, E., 1988, ApJ, 334, 252 (CMB88)
 Cisternas M. et al., 2011, ApJ, 726, 57
 Conroy C., Wechsler R. H., Kravtsov A. V., 2006, ApJ, 647, 201
 Conroy C., Wechsler R. H., 2009, ApJ, 696, 620
 Croton, D.J., et al. 2006, MNRAS, 367, 864
 Dahlen, T., Mobasher, B., Dickinson, M., Ferguson, H.C., Giavalisco, M., Kretchmer, C., Ravindranath, S., 2007, ApJ, 654, 172
 Dalla Vecchia C., Schaye J., 2008, MNRAS, 387, 1431
 Di Matteo T., Springel V., Hernquist L., 2005, Nature, 433, 604
 Dutton A. A., van den Bosch F. C., 2009, MNRAS, 396, 141
 Ellison S. L., Patton D. R., Mendel J. T., Scudder J. M., 2011, MNRAS, 418, 2043
 Faucher-Giguère C.-A., Quataert E., 2012, MNRAS, 425, 605
 Ferrarese L., Merritt D., 2000, ApJL, 539, L9
 Ferland, G.J., Porter, R.L., van Hoof, P.A.M., Williams, R.J.R., Abel, N.P., Lykins, M.L., Shaw, G., Henney, W.J., Stancil, P.C. 2013, Revista Mexicana de Astronomia y Astrofisica, 49, 1
 Fitzpatrick, E.L., Spitzer, L.J., 1997, ApJ, 475, 623
 Freyer T., Hensler G., Yorke H. W., 2006, ApJ, 638, 262
 Fynbo, J. P. U., Ledoux, C., Noterdaeme, P., et al., 2011, MNRAS, 413, 2481
 Fynbo, J. P. U., Geier, S. J., Christensen, L., et al., 2013, MNRAS, 436, 361
 Gabor J. M. et al., 2009, ApJ, 691, 705
 Gabor J. M. & Bournaud, F., 2013, MNRAS, 434, 606
 Gebhardt K. et al., 2000, ApJL, 539, L13
 Georgakakis A. et al., 2009, MNRAS, 397, 623
 Gerritsen J. P. E., Icke V., 1997, A&A, 325, 972
 Giavalisco, M., 2002, ARA&A, 40, 579
 Guo Q., White S., Li C., Boylan-Kolchin M., 2010, MNRAS, 404, 1111
 Grogin N. A. et al., 2005, ApJL, 627, L97
 Haardt, F., & Madau, P. 2012, ApJ, 746, 125
 Häring N., Rix H.-W., 2004, ApJL, 604, L89
 Heiles, C., 1990, ApJ, 354, 483
 Hellsten, U., & Sommer-Larsen, J., 1995, ApJ, 453, 264
 Hernquist L., 1989, Nature, 340, 687
 Hopkins P. F., Quataert E., Murray N., 2011, MNRAS, 417, 950
 Hopkins P. F., Keres, D., Onorbe J., Faucher-Giguère C.-A., Quataert E., Murray N., Bullock, J. S., 2014, MNRAS, 445, 581
 Hwang H. S., Elbaz D., Lee J. C., Jeong W.-S., Park C., Lee M. G., Lee H. M., 2010, A&A, 522, A33
 Jenkins, E. B., 2009, ApJ, 700, 1299
 Juneau S. et al., 2013, ApJ, 764, 176
 Katz N., 1992, ApJ, 391, 502
 Kawata D., Gibson B. K., 2003, MNRAS, 340, 908
 Kay S. T., Pearce F. R., Frenk C. S., Jenkins A., 2002, MNRAS, 330, 113
 Kennikutt, R. C. Jr, 1998, ApJ, 498, 541
 Kocevski D. D. et al., 2012, ApJ, 744, 148
 Koo, B.-C. & McKee, C. F., 1992, ApJ, 388, 93
 Krogager, J.-K., Fynbo, J. P. U., Møller, P., Ledoux, C., Noter-

- daeme, P., Christensen, L., Milvang-Jensen, B., & Sparre, M., 2012, MNRAS, 424, L1
- Landau, L.D., & Lifshitz, E.M., 1987, Fluid Mechanics, 2nd Edition, Pergamon Press: Oxford
- Laursen P., Sommer-Larsen J., & Andersen A.C., 2009, ApJ, 704, 164
- Leitherer C., Schaerer D., Goldader J. D., et al., 1999, ApJS, 123, 3
- Lia, C., Portinari, L., & Carraro, G. 2002a, MNRAS, 330, 821
- Lia, C., Portinari, L., & Carraro, G. 2002b, MNRAS, 335, 864
- Mac Low, M.-M. & Ferrara, A., 1999, ApJ, 513, 143
- Macciò A. V., Stinson G., Brook C. B., Wadsley J., Couchman H. M. P., Shen S., Gibson B. K., Quinn T., 2012, ApJL, 744, L9
- Marchesini D., van Dokkum P., Quadri R., et al., 2007, ApJ, 656, 42
- Marconi A., Hunt L. K., 2003, ApJL, 589, L21
- McCray, R., & Kafatos, M., 1987, ApJ, 317, 190
- McKee, C.F., & Ostriker, J.P., 1977, ApJ, 218, 148
- Møller, P., Warren, S. J., Fall, S. M., Fynbo, J. U., & Jakobsen, P., 2002, ApJ, 574, 51
- Monaghan, J. J., & Lattanzio, J. C. 1985, A&A, 149, 135
- Moster B. P., Somerville R. S., Maulbetsch C., van den Bosch F. C., Macciò A. V., Naab T., Oser L., 2010, ApJ, 710, 903
- Moster B. P., Naab T., White S., 2013, MNRAS, 428, 3121
- Murray N., Quataert E., Thompson T. A., 2010, ApJ, 709, 191
- Navarro J. F., Benz W., 1991, ApJ, 380, 320
- Newton R. D. A., Kay S. T., 2013, MNRAS, 434, 3606
- Noterdaeme, P., Petitjean, P., Carithers, W. C., et al., 2012b, A&A, 547, L1
- Oort, J.H., 1951, in Problems of the Cosmical Aerodynamics, (Dayton, Ohio: Central Air Document Office), p.118
- Oppenheimer B. D., Davé R., 2006, MNRAS, 373, 1265
- Ostriker, J.P., & McKee, C.F., 1988, Rev.Mod.Phys., 60, 1
- Pierce C. M. et al., 2007, ApJL, 660, L19
- Prochaska, X. J. & Stephane, H.-F., 2004, PASP, 116, 622
- Prochaska, X. J. & Wolfe, A. M., 2009, ApJ, 696, 1543
- Rahmati, A., Pawlik, A. H., Raicevic, M. & Schaye, J., 2013, MNRAS, 1000, 100
- Rauch, M., Haehnelt, M., Bunker, A., et al., 2008, ApJ, 681, 856
- Rauch, M. & Haehnelt, M. G., 2011, MNRAS, 412, L55
- Reddy, N. A. & Steidel, C. C. 2004, ApJ, 603, L13
- Richstone D. et al., 1998, Nature, 395, A14
- Roos O., Juneau S., Bournaud F., Gabor J. M., 2015, ApJ, 800, 19
- Salpeter, E.E., 1955, ApJ, 121, 161
- Sawala T., Guo Q., Scannapieco C., Jenkins A., White S., 2011, MNRAS, 413, 659
- Silk J., Rees M. J., 1998, A&A, 331, L1
- Scannapieco C., Tissera P. B., White S. D. M., Springel V., 2008, MNRAS, 389, 1137
- Scannapieco C., Wadepuhl M., Parry O. H., Navarro J. F., Jenkins A., Springel V., Teyssier R., Carlson E., Couchman H. M. P., Crain R. A., Vecchia C. D., Frenk C. S., 2012, MNRAS, 423, 1726
- Schawinski K., Simmons B. D., Urry C. M., Treister E., Glikman E., 2012, MNRAS, 425, L61
- Schaye J., Dalla Vecchia C., Booth C. M., Wiersma R. P. C., Theuns T., Haas M. R., Bertone S., Duffy A. R., McCarthy I. G., van de Voort F., 2010, MNRAS, 402, 1536
- Schechter, P., 1976, ApJ, 203, 297
- Schulze, S., Fynbo, J. P. U., Milvang-Jensen, B., et al., 2012, A&A, 546, A20
- Shapley, A. E., Steidel, C. C., Adelberger, K. L., Dickinson, M., Giavalisco, M., & Pettini, M. 2001, ApJ, 562, 95
- Shapley, A. E., 2011, ARA&A, 49, 525
- Somerville R. S., Primack J. R., 1999, MNRAS, 310, 1087
- Sommer-Larsen J., Götz M., Portinari L., 2003, ApJ, 596, 46
- Sommer-Larsen J., Romeo A.D., Portinari L., 2005, MNRAS, 357, 478
- Sommer-Larsen J., 2006, ApJ, 644, L1
- Sommer-Larsen J., Fynbo J.P.U., 2008, MNRAS, 385, 3
- Springel, V., & Hernquist, L., 2002, MNRAS, 333, 649
- Springel V., Hernquist L., 2003, MNRAS, 339, 289
- Stinson, G, Seth, A., Katz, N., Wadsley, J., Governato, F., & Quinn, T., 2006, MNRAS, 373, 1074
- Stinson G. S., Bailin J., Couchman H., Wadsley J., Shen S., Nickerson S., Brook C., Quinn T., 2010, MNRAS, 408, 812
- Stinson G. S., Brook C., Prochaska J. X., Hennawi J., Shen S., Wadsley J., Pontzen A., Couchman H. M. P., Quinn T., Macciò A. V., Gibson B. K., 2012, MNRAS, 425, 1270
- Stinson, G, Brook, C., Macciò, A.V., Wadsley, J., Quinn, T.R., & Couchman, H.M.P., 2013, MNRAS, 428, 129
- Thacker R. J., Couchman H. M. P., 2000, ApJ, 545, 728
- Torres G., 2010, AJ, 140, 1158
- van den Bosch F. C., Abel T., Croft R. A. C., Hernquist L., White S. D. M., 2002, ApJ, 576, 21
- Wang, L., Dutton, A. A., Stinson, G., Macciò, A. V., Penzo, C., Kang, X., Keller, B. W., & Wadsley, J., 2015, MNRAS, 454, 83
- Weaver, R., McCray, R., Castor, J., Shapiro, P., Moore, R., 1977, ApJ, 218, 377
- Weymann, R. J., Carswell, R. F., & Smith, M. G., 1981, ARA&A, 19, 41
- Wolfe, A. M., Gawiser, E., & Prochaska, J. X., 2005, ARA&A, 43, 861

APPENDIX A: MODELS OF THE GALAXY LUMINOSITY FUNCTION AT REDSHIFT 2.58

In general, the observational luminosity functions are well modeled by the Schechter (1976) law, $\Phi(L) = dN/dL = \Phi^* L^\alpha \exp(-L)$, where L is expressed in units of a characteristic luminosity L^* . Shapley et al. (2001) find, at $z \sim 3$, $\Phi^* = (6.2 \pm 2.7) \cdot 10^{-4} \text{ Mpc}^{-3}$, $\alpha = -1.85 \pm 0.15$ and $M_V^* = -22.98 \pm 0.25$. Marchesini et al. (2007) find, at $z \sim 3$, $\Phi^* = (16.3 \pm 4.6) \cdot 10^{-4} \text{ Mpc}^{-3}$, $\alpha = -1.12 \pm 0.24$ and $M_V^* = -22.77 \pm 0.22$. Finally, Marchesini et al. find, at $z \sim 2.25$, $\Phi^* = (11.6 \pm 2.9) \cdot 10^{-4} \text{ Mpc}^{-3}$, $\alpha = -1.02 \pm 0.21$ and $M_R^* = -22.67 \pm 0.21$. The LF of Shapley et al. is based mainly on LBGs (Lyman Break Galaxies), and is characterized by a steep faint end slope (e.g., Sommer-Larsen & Fynbo 2008). On the other hand, the LFs of Marchesini et al. are based on LBG samples, supplemented by DRG (distant red galaxies) samples. The faint end slopes of these LFs are considerably less steep than for the Shapley et al. The main reason for choosing these LFs is a desire to span a wide range of LFs in the analysis.

The above LFs are obviously *observational*, and it is well known that dust extinction plays a significant role in reducing the amount of light emitted by young galaxies, especially in the UV, e.g., Reddy & Steidel (2004), Dahlen et al. (2007). Since the extinction correction to the (UV based) co-moving star formation density is about a factor of 5.5 (e.g., Sommer-Larsen & Fynbo 2008), it is clear that even for (rest-frame) optical bands, like V and R, the correction is considerable. To estimate the extinction

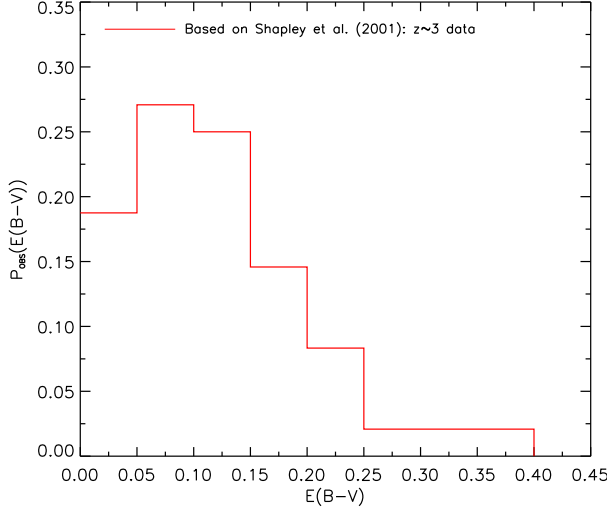


Figure A1. Observationally determined E(B-V) probability distribution, based on a subset of the Shapley et al. data. Note that, for illustrative purposes only, the probability distribution has not been appropriately normalized.

correction, we use the data of Shapley et al., who list values of E(B-V) for 72 galaxies. They find no correlation between *observed* M_V and E(B-V). In Fig. A1 we show the probability distribution $P_{obs}(E(B-V))$, based on the Shapley et al. data. Shapley et al. derive the E(B-V)s using population synthesis modeling. However, a number of their (bright) galaxies are assigned very young ages, typically a few tens of Myr. Such object are not seen in the simulations, so to be conservative we base the $P_{obs}(E(B-V))$ model on the 48 (out of 72) S01 galaxies of ages larger than 200 Myr — the simulated galaxies typically have mean ages of 0.5-1 Gyr.

In the following, the S01 observed LF is folded with the observed E(B-V) probability distribution, under the simplifying assumption that the observed M_V and observed E(B-V) are uncorrelated, as indicated by the S01 data. The relation between observed and de-reddened absolute V-band magnitude is given by

$$M_V = M_{V,obs} - A_V = M_{V,obs} - 4.05E(B-V) , \quad (\text{A1})$$

adopting a Calzetti dust law (Calzetti et al. 2000). From the definition of magnitude, this implies that the relation between the corresponding luminosities is given by

$$L_V = L_{V,obs} 10^{4.05 E(B-V)/2.5} = L_{V,obs} 10^{1.62\epsilon} , \quad (\text{A2})$$

where, for brevity, E(B-V) is denoted by ϵ . Alternatively, the ϵ that connects observed luminosity L_{obs} with intrinsic luminosity L (with $L \geq L_{obs}$), must be given by

$$\epsilon = \log\left(\frac{L_V}{L_{V,obs}}\right)/1.62 . \quad (\text{A3})$$

For a given $L_{V,obs}$, the number density of galaxies with observed luminosities in the small interval $[L_{V,obs}, L_{V,obs} + dL_{V,obs}]$ is given by $dN = \frac{dN}{dL_{V,obs}} dL_{V,obs}$. The fraction of these that have intrinsic luminosities in the interval $[L_V, L_V + dL_V]$ is given by

$$df = P_{obs}(\epsilon) d\epsilon = P_{obs}\left(\epsilon\left(\frac{L_V}{L_{V,obs}}\right)\right) \frac{d\epsilon}{dL_V} dL_V = P_{obs}\left(\epsilon\left(\frac{L_V}{L_{V,obs}}\right)\right) \frac{dL_V}{1.62 \ln(10) L_V} , \quad (\text{A4})$$

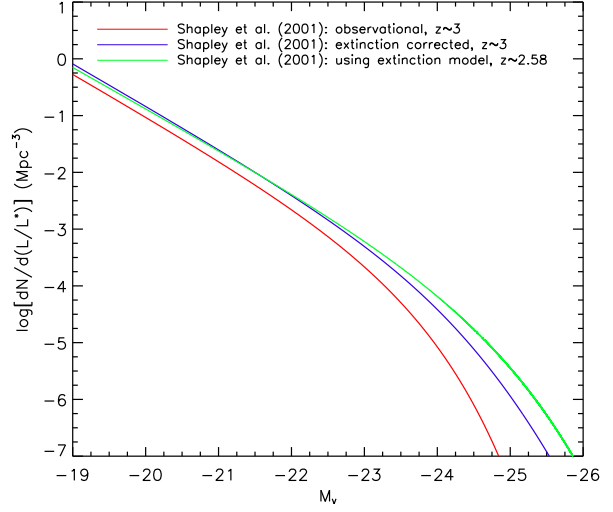


Figure A2. The observational $z \sim 3$ LF of Shapley et al. (2001) is shown by the red curve, together with the extinction corrected $z \sim 3$ LF, obtained as described in the text (blue curve), and with an extinction correction appropriate at $z=2.58$, as also described in the text (green curve).

where eq. (A3) has been used. Hence, the number density of galaxies with observed luminosities in the small interval of size $dL_{V,obs}$ and intrinsic luminosities in the small interval of size dL_V , can be expressed as

$$d^2 N = \frac{dN}{dL_{V,obs}} \cdot \frac{P_{obs}\left(\epsilon\left(\frac{L_V}{L_{V,obs}}\right)\right)}{1.62 \ln(10) L_V} dL_{V,obs} dL_V . \quad (\text{A5})$$

The extinction corrected LF is the obtained by integration over $L_{V,obs}$:

$$\frac{dN_{corr}}{dL_V}(L_V) = \int_0^{L_V} \frac{dN}{dL_{V,obs}} \cdot \frac{P_{obs}\left(\epsilon\left(\frac{L_V}{L_{V,obs}}\right)\right)}{1.62 \ln(10) L_V} dL_{V,obs} . \quad (\text{A6})$$

We now change variable in the integral in eq. (A6). It follows from eq. (A2) that $L_{V,obs} = L_V \cdot 10^{-1.62\epsilon}$, and hence that $dL_{V,obs}/d\epsilon = -1.62 \ln(10) L_V 10^{-1.62\epsilon}$. Eq. (A6) can then be rewritten as

$$\begin{aligned} \frac{dN_{corr}}{dL_V}(L_V) &= \int_{\epsilon_{max}}^0 \frac{dN}{dL_{V,obs}}(L_{V,obs}) \cdot \frac{dL_{V,obs}}{d\epsilon} \cdot \frac{P_{obs}(\epsilon)}{1.62 \ln(10) L_V} d\epsilon \\ &= \int_0^{\epsilon_{max}} \frac{dN}{dL_{V,obs}}(10^{-1.62\epsilon} L_V) P(\epsilon) 10^{-1.62\epsilon} d\epsilon , \quad (\text{A7}) \end{aligned}$$

where ϵ_{max} is the maximum observed value of E(B-V) - based on the data of S01, we set $\epsilon_{max}=0.4$ (see Fig. A1). Fig. A2 shows the result of applying the above procedure to the observational S01 $z \sim 3$ LF, together with the original S01 LF itself. If the observational LF is described by a power-law (i.e., scale-free), then, if the above approach is used, the extinction corrected LF will be a power-law with the same power index, just shifted towards larger L_V . Due to the “knee” of the luminosity function (caused by the exponential cut-off), however, the shapes of the observational and corrected LFs will be different, as can be seen from the Figure. In the same way, one can show that if the observational LF is described by a power-law, then the average E(B-V) of galaxies will be independent of uncorrected luminosity. This seems at odds with the fact

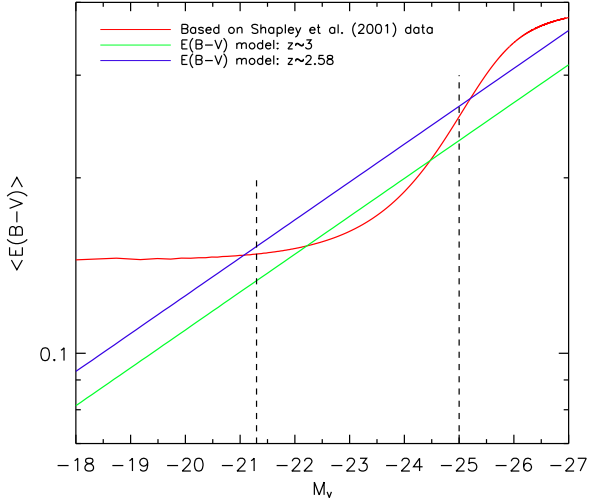


Figure A3. Average E(B-V) as a function of extinction corrected M_V .

that galaxy metallicity is correlated with luminosity, and it is typically assumed that the dust content in galaxies is correlated with the metallicity (e.g., Laursen et al. 2009). Due to the “knee” of the observational LF, however, extinction corrected luminosity is correlated with E(B-V), as one would expect — see Fig. A3, and also S01. As can also be seen from the figure, $\langle E(B-V) \rangle$ approaches a constant value for luminosities fainter than $M_V \gtrsim -22$ to -21 . This seems not physically reasonable (see above), and is a consequence of the assumption that E(B-V) is uncorrelated with observed luminosity (based on the S01 data in the limited range $M_{V,obs} \sim -21$ to -24), and the LF approximating a power-law at lower luminosities, cf. the discussion above.

In order to obtain a physically more reasonable extinction model, we consider the following model, where, for simplicity, E(B-V) is modeled as a *function* of M_V with the properties that a) E(B-V) decreases monotonically with decreasing intrinsic luminosity, and b) provides a good match to the S01 data over the limited M_V range available:

$$\log(\epsilon) = -0.065(M_V + 26) - 0.57, \quad z \sim 3, \quad (\text{A8})$$

where E(B-V), as before, is denoted ϵ . As can be seen from Fig. A3, the model provides a good match to the S01 data, in the limited range of M_V available.

The S01 LF is built on observations of $z \sim 3$ galaxies, so the above E(B-V) model obviously pertains to such a redshift. The DLA under discussion in this work is located at $z=2.58$, and the amount of heavy elements in galaxies will have increased during this ~ 400 Myr period. So when using the S01 observational LF model also as an observational LF at $z=2.58$, it is likely that a somewhat larger dust extinction correction is required to obtain the extinction corrected LF. To quantify this, we determined the metallicity of all simulated galaxies in this project, at both $z=3$ and $z=2.58$. We find an average increase in abundance at a given M_V of 0.06 dex or equivalently 15%. It is reasonable to assume that the average dust opacity has increased by a similar amount (e.g., Laursen et al. 2009), and, adopting a simple “screen” model, so has the average E(B-V). The final E(B-V) model adopted therefore reads

$$\log(\epsilon) = -0.065(M_V + 26) - 0.51, \quad z \sim 2.58. \quad (\text{A9})$$

This model is also shown in Fig. A3. In this paper, the extinction

corrected, $z=2.58$ LFs are determined on the basis of this model — see also below. It must hold that

$$\frac{dN_{corr}}{dL_V}(L_V) = \frac{dN}{dL_{V,obs}}(L_{V,obs}(L_V)) \cdot \frac{dL_{V,obs}}{dL_V}. \quad (\text{A10})$$

It follows from eq. (A2) that

$$\log(L_{V,obs}) = \log(L_V) - 1.62\epsilon. \quad (\text{A11})$$

Inserting the extinction model yields

$$\log(L_{V,obs}) = \log(L_V) - 1.62 \cdot 10^{-0.065(M_V + 26) - 0.51}. \quad (\text{A12})$$

Now, since in this work luminosities are expressed in units of L^* , it follows from S01, that $M_V = -22.98 - 2.5 \log(L_V)$. Inserting this in eq. (A12) yields

$$\log(L_{V,obs}) = \log(L_V) - 0.319 L_V^{0.163}, \quad (\text{A13})$$

which can be rewritten as

$$L_{V,obs} = L_V \cdot 0.48 L_V^{0.163}. \quad (\text{A14})$$

Taking the derivative of this equation results in

$$\frac{dL_{V,obs}}{dL_V} = 0.48 L_V^{0.163} (1.0 - 0.119 L_V^{0.163}). \quad (\text{A15})$$

Using eq. (A10), the final extinction corrected LF model can be expressed as

$$\frac{dN_{corr,1}}{dL_V}(L_V) = \Phi^* (0.48 L_V^{0.163} L_V)^\alpha \exp(-0.48 L_V^{0.163} L_V) (1.0 - 0.119 L_V^{0.163}), \quad (\text{A16})$$

where $\Phi^* = 6.2 \cdot 10^{-4} \text{ Mpc}^{-3}$, and $\alpha = -1.85$. This LF model is also shown in Fig. A2. As can be seen from the Figure, this LF is similar to the $z \sim 3$ one obtained by extinction correcting using the probabilistic approach described above (eq. (A7)), though at $M_V \lesssim -23$ the $z = 2.58$ LF model lies slightly above — this is due to the 15% larger dust opacity, as well as other differences between the two types of extinction corrections. For the purposes of this paper, the $z=2.58$ extinction corrections based on the probabilistic approach and on the extinction model (A9) lead to almost identical results — in this paper, model (A9) has been used exclusively.

The M07 $z \sim 3$ LF is also based on rest-frame V-band observations, and the extinction correction using the $z = 2.58$ extinction model (eq. (A9)) follows the same procedure as outlined above. The resulting extinction corrected LF is given by

$$\frac{dN_{corr,2}}{dL_V}(L_V) = \Phi^* (0.491 L_V^{0.163} L_V)^\alpha \exp(-0.491 L_V^{0.163} L_V) (1.0 - 0.116 L_V^{0.163}), \quad (\text{A17})$$

where $\Phi^* = 16.3 \cdot 10^{-4} \text{ Mpc}^{-3}$, and $\alpha = -1.12$. This LF model is also shown in Fig. A4. The M07 $z \sim 2.25$ LF is based on rest-frame R-band observations, and it is slightly more elaborate to perform the extinction correction using the $z = 2.58$ extinction model (eq. (A9)), which is based on the V-band absolute magnitude. We proceed as follows: For the simulated galaxies at $z = 2.58$, we find an average V-R of about 0.25 mag. For the purposes of the present work, we simply set $M_V = M_R + 0.25$. Substituting this into eq. (A9) yields

$$\log(\epsilon) = -0.065(M_R + 26.25) - 0.51, \quad z \sim 2.58, \quad (\text{A18})$$

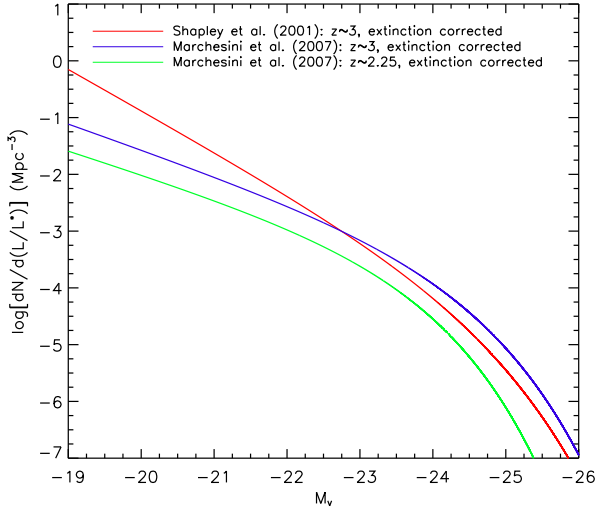


Figure A4. The three extinction corrected LFs, corrected using the $z = 2.58$ extinction model (eq. (A9)).

so $E(B-V)$ is now expressed in terms of M_R . For Calzetti dust (Calzetti et al. 2000)

$$M_R = M_{R,obs} - A_R = M_{R,obs} - 3.33E(B-V) . \quad (\text{A19})$$

Hence, by the definition of absolute magnitude it follows that

$$\log(L_{R,obs}) = \log(L_R) - 1.33\epsilon . \quad (\text{A20})$$

Inserting eq. (A18) in this yields

$$\log(L_{R,obs}) = \log(L_R) - 1.33 \cdot 10^{-0.065(M_R+26.25)-0.51} . \quad (\text{A21})$$

Now, as luminosities are expressed in units of L^* , it follows that $M_R = -22.67 - 2.5 \log(L_R)$ at $z \sim 2.25$ (Marchesini et al. 2007). Inserting this yields

$$\log(L_{R,obs}) = \log(L_R) - 0.24L_R^{0.163} , \quad (\text{A22})$$

which can be rewritten as

$$L_{R,obs} = L_R \cdot 0.575L_R^{0.163} . \quad (\text{A23})$$

Taking the derivative of this equation results in

$$\frac{dL_{R,obs}}{dL_R} = 0.575L_R^{0.163} (1.0 - 0.09 L_R^{0.163}) . \quad (\text{A24})$$

Finally, using the R-band equivalent of eq. (A10), the final extinction corrected LF model can be expressed as

$$\frac{dN_{corr,3}}{dL_R}(L_R) = \Phi^* (0.575L_R^{0.163} L_R)^\alpha \exp(-0.575L_R^{0.163} L_R) (1.0 - 0.09 L_R^{0.163}) , \quad (\text{A25})$$

where $\Phi^* = 11.6 \cdot 10^{-4} \text{ Mpc}^{-3}$, and $\alpha = -1.02$. This LF model is also shown in Fig. A4 — for comparison with the two other LF models, it is shown as a function of M_V , using $M_V = M_R + 0.25$ (see above).